Deformed Shape Calculation of a Full-Scale Wing Using Fiber Optic Strain Data from a Ground Loads Test

Christine V. Jutte, William L. Ko, Craig A. Stephens, John A. Bakalyar, W. Lance Richards, and Allen R. Parker

Dryden Flight Research Center, Edwards, California

December 2011

NASA STI Program ... in Profile

Since its founding, NASA has been dedicated to the advancement of aeronautics and space science. The NASA scientific and technical information (STI) program plays a key part in helping NASA maintain this important role.

The NASA STI program operates under the auspices of the Agency Chief Information Officer. It collects, organizes, provides for archiving, and disseminates NASA's STI. The NASA STI program provides access to the NASA Aeronautics and Space Database and its public interface, the NASA Technical Report Server, thus providing one of the largest collections of aeronautical and space science STI in the world. Results are published in both non-NASA channels and by NASA in the NASA STI Report Series, which includes the following report types:

- TECHNICAL PUBLICATION. Reports of completed research or a major significant phase of research that present the results of NASA Programs and include extensive data or theoretical analysis. Includes compilations of significant scientific and technical data and information deemed to be of continuing reference value. NASA counterpart of peer-reviewed formal professional papers but has less stringent limitations on manuscript length and extent of graphic presentations.

- TECHNICAL MEMORANDUM. Scientific and technical findings that are preliminary or of specialized interest, e.g., quick release reports, working papers, and bibliographies that contain minimal annotation. Does not contain extensive analysis.

- CONTRACTOR REPORT. Scientific and technical findings by NASA-sponsored contractors and grantees.

- CONFERENCE PUBLICATION. Collected papers from scientific and technical conferences, symposia, seminars, or other meetings sponsored or co-sponsored by NASA.

- SPECIAL PUBLICATION. Scientific, technical, or historical information from NASA programs, projects, and missions, often concerned with subjects having substantial public interest.

- TECHNICAL TRANSLATION. English-language translations of foreign scientific and technical material pertinent to NASA's mission.

Specialized services also include organizing and publishing research results, distributing specialized research announcements and feeds, providing help desk and personal search support, and enabling data exchange services.

For more information about the NASA STI program, see the following:

- Access the NASA STI program home page at *http://www.sti.nasa.gov*

- E-mail your question via the Internet to help@sti.nasa.gov

- Fax your question to the NASA STI Help Desk at 443-757-5803

- Phone the NASA STI Help Desk at 443-757-5802

- Write to:
  NASA STI Help Desk
  NASA Center for AeroSpace Information
  7115 Standard Drive
  Hanover, MD 21076-1320

NASA/TP—2011–215975
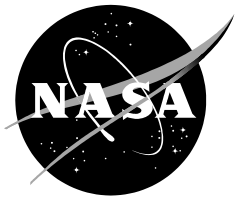
Deformed Shape Calculation of a Full-Scale Wing Using Fiber Optic Strain Data from a Ground Loads Test

Christine V. Jutte, William L. Ko, Craig A. Stephens, John A. Bakalyar, W. Lance Richards, and Allen R. Parker

Dryden Flight Research Center, Edwards, California

December 2011

Acknowledgements

The structural shape prediction method described in this report is protected under U.S. Patent No. 7,520,176, issued April 21, 2009. Therefore, those interested in using the method should contact the NASA Innovative Partnership Program Office at the Dryden Flight Research Center for more information.

Table of Contents

Abstract

A ground loads test of a full-scale wing (175-ft span) was conducted using a fiber optic strain-sensing system to obtain distributed surface strain data. These data were input into previously developed deformed shape equations to calculate the wing's bending and twist deformation. A photogrammetry system measured actual shape deformation. The wing deflections reached 100 percent of the positive design limit load (equivalent to 3 g) and 97 percent of the negative design limit load (equivalent to -1 g). The calculated wing bending results were in excellent agreement with the actual bending; tip deflections were within ±2.7 in. (out of 155-in. max deflection) for 91 percent of the load steps. Experimental testing revealed valuable opportunities for improving the deformed shape equations' robustness to real world (not perfect) strain data, which previous analytical testing did not detect. These improvements, which include filtering methods developed in this work, minimize errors due to numerical anomalies discovered in the remaining 9 percent of the load steps. As a result, all load steps attained ±2.7 in. accuracy. Wing twist results were very sensitive to errors in bending and require further development. A sensitivity analysis and recommendations for fiber implementation practices, along with, effective filtering methods are included.

Nomenclature

AFT	refers to a fiber on the aft part of the wing
AOI	angle of incidence
bottom	refers to a fiber on the bottom surface of the wing
c	distance between the neutral axis and the fiber of interest, in.
c_i	distance between the neutral axis and the fiber of interest at the i-th strain station, in.
c-ratio	the ratio of "c" values between the i-th and (i-th - 1) strain stations, (c_i/c_{i-1})
C	distance between the neutral axis and the fiber of interest.
d	chord-wise distance between the forward and aft fibers, in.
d_i	chord-wise distance between the forward and aft fibers at the i-th strain station, in.
DLL	design limit load
FBG	Fiber Bragg Gratings
FOSS	fiber optic strain sensing
FWD	refers to a fiber on the forward part of the wing
GRF	ground reference frame, aligns with the global y-direction (up)
h	distance between corresponding top and bottom fibers measured in the wing's out-of-plane direction, in.
h_i	distance between corresponding top and bottom fibers measured in the wing's out-of-plane direction at the i-th strain station, in.
i	= 0,1,2,3,…n, strain station index numbers
Inf	infinity
m	gradient between two adjacent slope values (calculated at the strain stations) of the deformed wing
n	Index for the last strain station
NaN	not-a-number
NASA	National Aeronautics and Space Administration
out-of-plane	direction perpendicular to a wing's neutral axis in bending
RMSE	root-mean-square error
RRF	rotated reference frame, aligns with the wing's out-of-plane direction
tol	tolerance
top	refers to a fiber on the top surface of the wing

x_i	spanwise distance between the wing's centerline and the i-th strain station, in.
y_i	vertical (out-of-plane) deflection at the i-th strain station, in.
Δl	distance between two adjacent strain stations, in.
ε_i	strain at the i-th strain station
θ_i	slope of wing (in the spanwise direction) at i-th strain station, radians or degrees
ϕ_i	cross-sectional wing twist angle at the i-th strain station, radians or degrees

Introduction

The objective of this effort was to experimentally validate equations that translate structural surface strains, on a wing for example, into numerous single point vertical (out-of-plane) displacements along the wing for wing shape (bending and twist) calculation (refs. 1–5). These deformed shape equations are meant to be used for real-time shape sensing during flight. Up to this point, the equations have only been verified using strain data from a finite element analysis model and minimal (small loads and displacements) experimental testing (ref. 6). Experimental validation of these equations required a physical full-scale wing loading over the wing's entire range of motion, a high density of structural surface strain measurements along the wing, and measurement of the wing's actual deformation under load. These requirements were met by implementing a fiber optic strain-sensing (FOSS) system on a full-scale ground loads test of a large span wing from an unmanned aerial vehicle, the Global Observer (AeroVironment, Incorporated, Monrovia, California) (fig. 1). Fiber optic strain data collected during wing load testing served as input into the deformed shape equations (ref. 4), which calculated wing bending and twist deformation. The accuracy of the wing shape calculations is based on a comparison with the wing's actual shape deformation measured by a photogrammetry system.

Fiber optic sensors have various features, including the capability of providing a high density of strain measurements on a structure. Aerospace applications can benefit from the installation of FOSS technology. With validation of the deformed shape equations, wing shape measurements can be exploited to enable lighter weight aircraft by providing feedback for aeroelastic wing shape control. For example, mishaps like the Helios vehicle, which was a flexible, large-span flying wing that broke apart during flight in June 2003, may have been avoided with shape feedback (ref. 7). For supersonic aircraft, shape control may also lessen the intensity of a sonic boom (ref. 8). In addition, the high density of strain measurements provided by FOSS enables an additional validation tool for aircraft structural models. Besides aerospace, these attributes of shape and strain sensing are transferable to other sectors such as medical devices, space structures, and large civil structures.

The optical fibers used in this testing have strain sensors, called Fiber Bragg Gratings (ref. 9 and 10), located at every half inch along their length. For this reason, the sensing capability is multiplexed, meaning that many strain readings can be taken via a single optical fiber, which enables a lightweight distribution of sensors. Figure 2 shows strain gages and fiber installed on the Global Observer for this testing. Compared to the optical fiber, strain gages have much wider footprints and require numerous leads from each gage, which add extra weight and volume. Unlike most sensors, the fiber is immune to electromagnetic interference, radio frequency interference, and radiation. When recording data during flight, the FOSS system flown on the Global Observer is capable of measuring strain data at 60 samples per second for 8 fibers, where each fiber has up to 40 ft of sensing length which includes 960 strain sensors. That means 7680 strain readings are processed per flight system at a rate of 60 Hz. Improvements to the system are continually being made to provide more sensing capabilities at even higher rates.

This report explores the accuracy of the deformed shape calculations over a wing's entire range of motion using a full-scale structure and empirical data from the FOSS measurements. Actual wing deformation data is acquired for comparison purposes. The report is organized as follows. First, background for the full-scale ground loads test including the implementation of FOSS and the structural shape calculation equations is provided. Second, the results of the wing bending and wing twist calculations are presented. Third, improvements to the shape calculation making it more robust to the inherent variations of empirical data are offered. Fourth, a sensitivity analysis using some of the parameters that potentially affect the wing shape results is described. Finally, the report summarizes the conclusions and makes recommendations for how to best implement the fiber on a structure, along with which filtering methods to use with the deformed shape equations to attain the most accurate results. Additional future potential upgrades to the FOSS system to improve system capabilities are also described.

Ground Loads Testing Using FOSS

Test Description

A full-scale ground loads test was performed on a wing from the Global Observer, a high-altitude long-endurance unmanned aerial vehicle. The Global Observer's wing is all-composite and spans 175 ft. As shown in figure 1, the wings are unswept and have a slight dihedral and taper near the wing tip. Structural load tests of a full-scale Global Observer wing were conducted at the National Aeronautics and Space Administration (NASA) Dryden Flight Research Center's Flight Loads Laboratory in the summer of 2010. Figure 3 shows the left wing during one of the test conditions with a distributed load applied to the wing using a whiffletree arrangement. The entire wingspan was loaded; however, only the left wing was instrumented to determine the accuracy of the wing shape calculations. The fuselage was not included during the test; instead, the centerline of the wingspan was fixed, such that every load step had a zero displacement and slope at the centerline of the wingspan. The primary goal of the test was to determine the structural integrity of the wing; whereas, the data collection for fiber optic wing shape calculations was a secondary objective but provided a unique opportunity to evaluate the FOSS derived wing shape sensing methodology developed at NASA Dryden under controlled loading conditions.

The data used for this report were based on two test set-ups. The first test installed the wing at an 11° angle of incidence and applied a distributed load to 100 percent of the positive design limit load (DLL), which corresponded to +3 g. The second test installed the wing at a 6° angle of incidence and applied a distributed load to 97 percent of the negative DLL, which corresponded to -1 g. During, the negative load testing, shot bags were used along with the whiffletree to provide the appropriate loading. For each test, load steps were increased by 10-percent DLL until reaching the maximum DLL, and then decreased by 10-percent DLL until the wing returned to its original position.

Data Collection

In order to calculate wing shape during the positive and negative load cases, a high density of structural surface strain measurements, acquired by a NASA Dryden in-house developed FOSS system, along with external wing geometry was gathered. The wing geometry was provided by AeroVironment using data based on wing models. Conventional electrical resistance strain gages were used to validate the FOSS strain measurements. To assess the performance of the wing shape calculation, the wing's actual deformation was measured using a photogrammetry system.

The deformed shape equations assume out-of-plane displacements are perpendicular to the wing's neutral axis. For a given angle of incidence of the wing, the neutral axis will rotate with the wing. Figure 4 shows the two coordinate systems used in this testing. The y-direction of the ground reference frame

(GRF) aligns with the global vertical direction, whereas the y'-direction of the rotated reference frame (RRF) aligns with the wing's out-of-plane direction, which is oriented perpendicular to the wing's installed angle of incidence. The deformed shape calculations are made in the RRF. Since the photogrammetry data were recorded in the GRF, this data were reoriented to the RRF for comparison purposes. The x-direction of both reference frames is oriented spanwise along the wing. Figure 4 also shows the positive direction for the calculated twist angle using the deformed shape equations.

Fiber Optics

For the ground loads test, four spanwise optical fibers were positioned on the wing surface near the centerlines of the forward and aft spars, yielding over 7500 fiber optic strain sensors. Figure 4 shows a typical cross-section of how the four fibers were positioned and numbered for this test. Due to the wing's large span, it was constructed in separate sections. Thus, each of the four spanwise fibers consisted of three individual fibers as shown in figure 5 with short gaps in between to exclude locations where the separate parts of the wing were joined. On both the top and bottom surfaces, the aft fiber had to taper in slightly to conform to the wing's geometry.

Strain Gages

Conventional foil strain gages were installed adjacent to the optical fibers at various locations as a means of validating the fiber optic strain readings (fig. 2). These measurements were only used for structural evaluation, not for shape calculation. The spanwise locations of the strain gages relative to a single fiber will be illustrated in a later section.

Photogrammetry

A photogrammetry system (a PONTOS 5M system configuration by GOM® Optical Measuring Techniques, Braunschweig, Germany) (ref. 11) was utilized to provide the validation displacement information for the wing shape calculation. Photogrammetry targets (shown in figure 3) were positioned on the upper surface of the left wing approximately every 2 ft down the wingspan and closely located above the forward and aft spars. For visibility the targets stand upright and perpendicular to the wing surface, as seen in figure 3 (b). The photogrammetry data provide information of each target position relative to one another and also each target's spatial displacement vector relative to its initial position at 0-percent DLL. For each load step, ten photogrammetry images were taken over an 18-20 s time period. The accuracy of this system for the configuration used during this testing was approximately 1/32 in.

Approach to Calculating Deformed Shape

Equations (1–5) (ref. 4) developed previously were used to transform the measured surface strains into out-of-plane displacements at numerous single-point locations on the wing. By calculating these displacements at enough points along the wing, the wing's bending can be approximated by comparing the individual displacements in the wing's spanwise direction, while the twist can be approximated by comparing the displacements in the wing's chordwise direction. In this work, wing shape is defined as the combination of both wing bending and twist. Strain data is measured using four spanwise fiber runs (two fibers on the top surface and two fibers on the bottom surface).

Equations (1) and (2) are referred to as the displacement transfer functions, which convert surface strains into out-of-plane displacements, y_i, where "i" represents a particular location along the span of the wing, which is referred to as a strain station. Figure 6 shows how the Global Observer wing was broken down into various strain stations. Equations (1) and (2) were specifically developed for slightly non-uniform (that is, slowly changing cross-section) cantilever beams. These equations apply to a single set of

4

spanwise strain data, such that when using fiber optics, it is equivalent to finding the wing displacement along a single fiber. Each individual displacement value, y_i, is calculated using information from inboard strain stations.

Displacement equation (called Deflection Equation in reference 4):

$$y_i = \frac{(\Delta l)_i^2}{6c_{i-1}}\left[\left(3 - \frac{c_i}{c_{i-1}}\right)\varepsilon_{i-1} + \varepsilon_i\right] + y_{i-1} + (\Delta l)_i \tan\theta_{i-1}, \quad (i = 1,2,3,....,n)$$ (1)

[...........1st Term..............] [2nd] [...3rd Term...]

Slope equation:

$$\tan\theta_i = \frac{(\Delta l)_i}{2c_{i-1}}\left[\left(2 - \frac{c_i}{c_{i-1}}\right)\varepsilon_{i-1} + \varepsilon_i\right] + \tan\theta_{i-1}, \quad (i = 1,2,3,....,n)$$ (2)

Spanwise strain data is interpolated at each strain station. The value "$(\Delta l)_i$" represents the distance between adjacent strain stations and is calculated as follows.

Distance between strain stations equation:

$$(\Delta l)_i = x_i - x_{i-1}, \quad (i = 1,2,3,....,n)$$ (3)

where the x-direction aligns in the spanwise direction from centerline (or root) to tip. For the Global Observer, the (Δl)'s were uniform, except at the wing's two connecting joints, where a gap occurred between the spanwise fibers. At these locations, Δl was larger to exclude wingspan that did not measure strain data as shown in figure 6.

The value "c_i" in equations (1) and (2) is the distance between the wing's neutral axis and the location on the wing where strain reading (ε_i) is taken. Figure 7 illustrates the "c" values for a single cross-section with respect to the cross-sectional thickness "h" between an upper and lower strain reading. The "c_i" values for the top and bottom surfaces are calculated as follows.

"c" value equations:

$$c_{top,i} = \frac{\varepsilon_{top,i}}{\varepsilon_{bottom,i} - \varepsilon_{top,i}} * h_i, \; c_{bottom,i} = \frac{\varepsilon_{bottom,i}}{\varepsilon_{bottom,i} - \varepsilon_{top,i}} * h_i, \quad (i = 0,1,2,....,n)$$ (4)

Given equation (4), no knowledge of the wing's neutral axis location is needed prior to testing, because the location can be determined experimentally. However, if accurate knowledge of the wing's neutral axis location is available, it is possible to calculate wing shape with only two fibers (either on the top surface or the bottom surface), but the accuracy of this approach was not examined within this report, since the location of the wing's analytical neutral axis was not available.

To calculate wing twist, displacement information from two fibers on the same surface is used to calculate the cross-sectional twist angle, ϕ_i, where,

Cross-sectional twist angle equation:

$$\phi_i = \sin^{-1}\left(\frac{y_{i_{FWD}} - y_{i_{AFT}}}{d_i}\right), \quad (i = 0,1,2,....,n) \tag{5}$$

Dimension "d_i" represents the chord-wise distance between the forward and aft fibers at station (i). Figure 8 shows that ϕ_i represents the twist angle at strain station (i), where "d" is now tilted due to wing twist.

To summarize, figure 9 describes the general approach for the deformed wing shape calculation. Although surface strain measurements can be made by other techniques, such as finite element analysis and strain gages, FOSS is an enabling technology that makes real-time in-flight shape determination practical because it provides a high-density of distributed surface strain measurements at a minimal weight penalty.

Application of the Deformed Wing Shape Equations

The method for determining wing shape depends heavily on the validity of the FOSS measurements since these data are used as input to the deformed shape equations. Figure 10 shows typical strain data as a function of span locations on the Global Observer wing; the strain data was normalized for one of the four spanwise fibers. The strain data from individual Fiber Bragg Gratings (FBG)s closely compare to the strain gage measurements. For this ground test, the FBG strains were time averaged over 18-20 s, while a load step was held constant. These time-averaged values were then interpolated at chosen strain stations along the wingspan and used in the deformed shape equations. The resulting displacements were compared to a single photogrammetry image to determine the accuracy of the shape calculation for each constant loading step. For this test, one of the fibers was determined to have a 4.5-ft span of unreliable data near the wing's mid section due to a fracture in the fiber. Within this region, the strains were linearly interpolated at each strain station using strain data measured immediately before and after this unreliable data.

In calculating the wing displacement, the first strain station (i=0) must have strain data available and a known (not calculated) displacement and slope over the wing's range of motion. The wing root, or centerline in the case of this ground loads test, always has a zero displacement and slope, and is typically chosen for the first strain station; however, for this ground test, the fibers did not extend to the centerline and no strain gage was installed there either. Additionally, accurate extrapolation of strain data to the centerline was not possible. Thus, the first strain station could not be located at the centerline; therefore, it was located at the first photogrammetry station outboard of the centerline for the positive load case. This photogrammetry station was at a span location of 65.77 in. from the centerline (x = 65.77 in.), where optical fibers were also located. At this span location, the out-of-plane displacement is directly available from the photogrammetry data. The slope information is not available; however, the slope immediately before and after this location can be calculated using the photogrammetry data (including the wing's out-of-plane displacements) of the wing's first three photogrammety stations, which were located at x = 0, 65.77, and 90.95 in. Thus, the slope at x = 65.77 in. was calculated by taking the average of the slope between x = 0 and 65.77 in., and the slope between x = 65.77 and 90.95 in. For the negative load case,

6

photogrammetry data was not available at x = 65.77 in., but at x = 40.82 and 91.31 in. Therefore, the displacement at x = 65.77 in. was calculated using linear interpolation, and the slope was calculated as the slope between x = 40.82 and 91.31 in.

Wing Bending and Twist Results

This section presents the results for the wing shape calculation of the Global Observer over the range of motion resulting from +3 to -1 g load conditions. For these calculations, the distance chosen between strain stations, Δl, was 6 in.; however, as previously mentioned, the Δl's were larger at the two wing joints since no strain data was available there. Results are only shown for fibers 3 and 4, since FOSS has the capability of revealing proprietary information about the structure's internal properties when data from all 4 fibers are analyzed. Even though the displacement calculations from fibers 1 and 2 are not provided, the displacement and rotation calculations of fibers 3 and 4 still depend on the strains from fibers 1 and 2.

Out-of-Plane Displacement (Bending) Calculation

By calculating the wing's out-of-plane displacement at distributed points along the wingspan, the wing's bending deformation is determined. The results for both the positive and negative load cases are given below.

Positive Loading Case

For the positive load case, 100-percent DLL corresponds to a +3 g loading condition. Figures 11 and 12 compare the out-of-plane displacement calculation to the actual displacement for fibers 3 and 4, respectively. The actual displacement is measured by the photogrammetry targets, whose locations along the wingspan are indicated by the circles in the figures. The photogrammety data is only shown in the RRF since this was the frame used to compare the results; furthermore, when data from both reference frames was originally plotted, the offset between the RRF and the GRF was almost undetectable. Figures 11 and 12 both show that the calculated displacements closely match the actual displacement for every load step, 0 to 100-percent DLL.

Figures 13 and 14 examine the displacement error at the wing tip at a span location of 1025 in. (85.4 ft) from the wing's centerline, which is only 2.1 ft from the wing tip. This location was selected since it is one of the most outboard photogrammetry stations that had fiber optic strain data available for all four fibers. Both figures provide displacement error over the entire positive loading from 0-percent DLL to 100-percent DLL then back down to 0-percent DLL.

The displacement error was calculated as shown in equation (6),

$$error = calculated - actual \text{ (that is, photogrammetry results in the RRF)}, \tag{6}$$

such that an under-prediction in terms of inches or percent error will have a negative number. Figure 13 shows the error in terms of inches. The calculated displacements of the wing tip measured at the 1025-in. span location was within ±2.5 in. of the actual displacement over the entire load cycle, where the maximum displacement at this span location was 155 in. (13 ft). Figure 14 shows displacement error in terms of percent error. At smaller load conditions (less than 20-percent DLL), the percent errors are larger since the wing tip deflections are smaller; for example, at 10-percent DLL, the tip displacement was approximately 16 in., whereas the displacement was 155 in. (13 ft) at 100-percent DLL. Since the displacement at 0-percent DLL is zero, or a very small number, the percent errors in displacement

approach infinity. This same trend occurs when comparing the percent errors along a wingspan at a constant load step. Figure 15 shows the results of the 100-percent DLL load case. Near 25-, 50-, 75-, and 100-percent span, the max absolute displacement error is 1.3 in. However, when comparing the corresponding percent errors at each of these span locations, the magnitudes are larger near the wing root, since the wing displaces less near the root. For this reason, most of the results shown in this report will be provided in both inches error and percent error, since at times one or the other may be a better representative metric of the calculation's performance.

Negative Loading Case

For the negative load case, 100-percent DLL corresponds to a -1 g loading. Figures 16 and 17 compare the out-of-plane displacement calculation to the actual displacement for fibers 3 and 4, respectively. Both figures show that the calculated displacements closely follow the actual in most cases; however, some discontinuities are detected in the displacement calculations near the wing tips. This occurs at 60-percent DLL for fiber 3 and 40- and 50-percent DLL for fiber 4. These discontinuities more commonly occur in lower strain regions, which correlate well with the discontinuities in these figures, since the strains are much lower near the wing tip. The next section will show that these discontinuities are errors due to numerical anomalies that can occur when empirical strain data are fed into the deformed shape equations. Methods will be proposed that address these discontinuities.

Like the positive loading case, error is calculated using equation (6); however, this means that an under-prediction will have a positive number in terms of inches but a negative number in terms of percent. Figures 18 and 19 examine the error at the wing tip. Again, the error was measured at a span location of 1025 in. (85.4ft) from the wing's centerline, which is only 2.1 ft from the wing tip. The maximum out-of-plane displacement was approximately -46 in. (-3.8ft). Both figures only cover the data collected while the load was increasing, since the individual load steps were not as clearly defined while the wing load was decreased from -97 to 0-percent DLL due to the required test procedures. Figure 18 shows the wing tip displacement error in terms of inches, while figure 19 shows the percent error. With the exception of the circled results, which correspond to discontinuities shown in figures 16 and 17, the calculated displacements of the wing tip measured at the 1025-in. span location was within ±2.7 in. of the actual displacement. Besides the occurrence of discontinuities (circled results), the percent errors are the same or slightly worse than the errors seen in the positive loading case for similar loading magnitudes, where 33 percent of the positive DLL corresponds to 1 g. In no instance is the difference in percent errors between the positive and negative loading cases larger than 5 percent.

Wing Twist Calculation

The wing displacement calculations for fibers 3 and 4 were used to calculate the wing twist (eq. (5)). Figures 20 and 21 compare the calculated wing twist to the actual wing twist measured at a span location of 1025 in. (85.4ft) from the wing's centerline. The largest actual wing tip rotations were -0.4° (at 100-percent DLL) for the positive load case and 0.2° (at 97-percent DLL) for the negative load case. The results can be summarized by looking at the wing twist error calculated using equation (6). Figures 22 and 23 show the resulting errors in twist calculation for both the positive and negative load cases, respectively. Disregarding the circled errors in wing twist, which correspond to the occurrences of discontinuities in the displacement calculation, the absolute errors in wing twist are seen as large as 6°. Therefore, even though the displacement errors at the wing tip were relatively small compared to the maximum deflection of 13 ft, a few inches of error on both the forward and aft fibers can cause large errors in wing twist since the distance between the two fibers (d in eq. (5)) is relatively small because it must be less than the wing's chord length. An illustration of the affect displacement errors have on twist

8

is shown in figure 24. Hence, this method of calculating wing twist using fiber optic strains requires further development.

Handling Empirical Data

When using empirical data, several numerical anomalies can disrupt the deformed wing shape calculations. If a strain value is determined to be zero (exact/perfect zero), the calculated displacement can be indeterminate. Another numerical anomaly exists when the distance from the fiber to the neutral axis ("c") is very large or very small. This condition can create a discontinuity in the calculated slopes and displacements of the wing, leading to additional errors. Different methods for addressing these anomalies are discussed in the following sections.

Perfect-Zero Anomaly

The FOSS system records strains as integers with units of microstrain. Therefore, very small strains are recorded as perfect zeros. When these zeros are fed into the displacement equations, the calculated displacement can be indeterminate, due to division by zero in the denominator of the displacement equation via the "c" values. Software updates to the FOSS system can be made to record strains as floating-point numbers; however, the value of this modification is limited since the system typically has a noise floor greater than a couple microstrain, giving integer values sufficient accuracy.

To eliminate a division by zero, modifications can be made to either the strain data or the "c" data. Through a study, it was found that changing all the perfect-zero strains to a constant (a small value) did not always eliminate problematic "c" values, since these constants sometimes appeared as both strain values in the denominator of the "c" equation (eq. (4)), creating another perfect zero in the denominator. Conversely, the perfect-zero anomaly was eliminated by directly modifying the "c" values. In Matlab® (The MathWorks, Natick, Massachusetts), a problematic "c" value is detected as either a perfect zero, "NaN" (not-a-number when a zero is divided by zero), "Inf" (positive infinity for a positive number divided by zero), or "–Inf" (negative infinity for a negative number divided by 0). Specifically, the "c" values were modified as follows:

1. c = 0 or NaN → c= small constant (0.1 inches in this work),
2. c = Inf → c = large positive constant (100 inches in this work),
3. c = - Inf → c = large negative constant (-100 inches in this work).

The values chosen for the constants were not formally optimized. The large "c" values used for the constants may not seem realistic considering the wing thickness of most aircraft, but the objective is to modify the infinite "c" values to enable calculation of displacement, while also representing the large "c" values calculated from the empirical strain data. Even when no perfect zeros appear in the strain data, it is not uncommon for large, unrealistic "c" values to be calculated from the empirical strains. These values potentially pose a problem in the displacement calculation, as described in the next section.

As a final note, the perfect-zero anomaly did not disrupt the displacement and twist results shown in the previous section of this paper since the strain data was time averaged over 18-20 s (the time duration that 10 photogrammetry images were taken), making the appearance of a perfect-zero less likely.

C-Anomaly

The "Wing Bending and Twist Results" section showed that discontinuities could sometimes appear in the displacement results (as circled in figures 16 and 17). Figure 25 (a) depicts another example where

a similar discontinuity occurred. With further investigation, it was found that the locations of these discontinuities correlate with discontinuities in the slope equation (eq. (2)). Figure 25 (b) plots the calculated slope versus the wingspan. The "c" values generated from empirical strain data are used as inputs to the slope equation and can greatly affect its continuity. Very large "c" values can occur when the two strains in the "c" equation's denominator, (ε_{bottom} - ε_{top}), in equation (4) are close to identical. Very small "c" values can occur when an extremely small strain is located in the numerator of the "c" equation. Also, additional discontinuities have been discovered by plotting the "c_i/c_{i-1}" component of the slope equation, as shown in figure 25 (c). By plotting strains versus span, it is not clear where a c-anomaly will occur; however, these anomalies typically occur in regions where the strain values are close to zero. It is in these regions that strain values can either be very small (creating a small "c" value) or almost identical between the upper and lower strains (creating a large "c" value).

These "c" values not only affect the slope portion of the displacement equation (shown as the third term of eq. (1)), but they also affect the first term in the displacement equation, which contains three "c" values. However, when detecting discontinuities in the displacement calculation, it is helpful to consider the slope portion of the equation, since it has a physical representation of the structure. For example, unless the wing breaks (for which the fibers would likely break also), there should be no discontinuity (or kink) detected in the wing's spanwise slope.

Eliminating Discontinuities

To make the displacement equations more robust to empirical strain data, five methods have been developed, each of which eliminate perfect zeros from the strain data and minimize the occurrence of problematic "c" values. Details about the implementation of each method are available in Appendix A. The first method, the Check Load method, uses a constant set of "c" data that is acquired from a check load applied to the structure before flight. This data is filtered and then curve-fit before use in the deformed shape equations. The remaining four methods calculate the "c" values of the structure using the real-time, empirical strains, and also detect and eliminate strain stations with problematic "c" values. The sensitivity of detecting a problematic "c" value is dependent on a tolerance level chosen by the user, as described in Appendix A. When a strain station is eliminated, the strain values and "c" values corresponding to that strain station are not used in the calculations. An elimination is accounted for by using a larger Δl to "skip" over the eliminated strain stations and quantify the distance between the remaining, newly adjacent strain stations. The Discontinuous C Filter and the Curve-fit Discontinuous C Filter methods eliminate strain stations that have "c" values that are either large or create a discontinuity in the spanwise calculation of the c-ratio, c_i/c_{i-1}. The Discontinuous Slope Filter and the Curve-fit Discontinuous Slope Filter methods eliminate strain stations that have "c" values that cause discontinuities in the wing's spanwise slope calculation. In particular, the Curve-fit Discontinuous C Filter and the Curve-fit Discontinuous Slope Filter methods include an additional step by curve fitting the filtered "c" data and solving for the "c" values at each original strain station location, such that no strain station is ultimately eliminated.

A Comparison Study Using the Proposed Methods

It is obvious that each of these methods will have differences in computational efficiency, especially for the Check Load method which uses predetermined "c" values. However, none of these methods have been formally optimized for mathematical or computational efficiency. Also, the current fiber optic strain sensing systems have a significant amount of available processing power, making all of these methods potentially real-time algorithms. For these reasons, the methods will not be compared based on computational efficiency.

10

One way to determine a method's robustness is to use it to calculate wing displacement multiple times, each time using a different Δl, recalling that Δl is the distance between strain stations. Since the Global Observer has a half-span of 87.5 ft, there should not be a large change in the displacement calculation when using Δl s of 1-, 4-, 6-, or 12-in. length; evidence of this will be shown in a sensitivity analysis later in the report. These changes in Δl, however, cause the strain data to be interpolated at different points along the wingspan, which changes the resulting strains, "c" values, and c-ratios. The displacement calculations using the four different Δl values should be fairly consistent, unless one calculation encounters a discontinuity. This discontinuity would be detectable as a larger, inconsistent error compared to the calculations using different Δl s and would increase the root-mean-square error (RMSE) over the four calculations.

Comparison Study – In this study, seven load steps were chosen which covered the wing's full range of motion at -97, -50, -10, 0, 10, 50, and 100 percent DLL. The five individual methods were first compared to one another over a single load step (for example, -97 percent DLL), so that each method was utilizing the same set of strain data. The RMSE for each individual method was calculated using the results of four displacement calculations each having a different Δl value of approximately 1, 4, 6, or 12 in. in length. Once every method had an RMSE value for each of the seven load steps from -97 to 100 percent DLL, these RMSE values were used to compare methods as a whole looking for potential trends that help determine which method is most effective.

Results – Tables 1 and 2 show the results of this study for fibers 3 and 4, respectively. Table 1a shows individual displacement errors at the wing tip (at a span location 1025 in. from the centerline) that were calculated directly from the unfiltered data; that is, none of the five filtering methods were used to produce these results. There are a total of 28 displacement errors (4 different Δl 's used over 7 different load steps.) Inconsistencies in the results become apparent when comparing errors within each column. A larger, outlying error is usually an indication of a displacement calculation that had a discontinuity issue. These outlying errors are boxed in tables 1a and 2a for reference.

The row labeled "No filter" in table 1b shows the RMSE for each load step (or column) in the top half of the table (inches are used for the RMSE since the errors at 0-percent DLL can throw off the comparison). By looking across the row, the larger RMSE values indicate when a discontinuity problem occurred. Using each of the five proposed methods, the same 28 displacement calculations were calculated and then summarized using the RMSE value for each of the seven load steps. Those values are found in the 2nd to 5th rows of data in tables 1b and 2b. By comparing the RMSE values within a single column, the lower RMSE values indicate that a discontinuity problem was eliminated by the corresponding method. The lowest RMSE value in each column is underlined for reference. It is also important to check that even when the non-filtered data did not encounter a discontinuity problem, that the methods do not somehow add more error to the calculation.

Discussion – In tables 1a and 1b (fiber 3), the higher RMSE value for the non-filtered data indicated discontinuity problems at -97 and 10-percent DLLs. By looking at the RMSE values of the five filtering methods, each method has a substantially lower RMSE value, indicating that the discontinuity problem was eliminated. Overall, the filtering methods typically showed improvement in the RMSE. The Curve-fit Discontinuous Slope Filter method had a large (147.93 in.) RMSE for the 0-percent DLL load step. With further investigation, it was found that a curve-fit through "c" values for one of displacement calculations passed through zero, causing a large c-ratio value. Overall, the Check Load and Curve-fit Discontinuous C Filter methods performed the best.

In tables 2a and 2b (fiber 4), the methods typically showed improvement in the RMSE over the non-filtered data, especially for the 0 and 10-percent DLL load steps where discontinuities were originally a

problem. At 50-percent DLL, the Curve-fit Discontinuous Slope Filter method had another relatively large (6.44 in.) RMSE compared to the other values within the column. At the extreme load cases, the Check Load method also had relatively higher RMSE values than the other methods. The Discontinuous Slope Filter, Discontinuous C Filter, and Curve-fit Discontinuous C Filter methods all performed similarly and had the lowest average RMSE's.

In tables 1 and 2, the "Ranking" column shows that the Check Load method performed either first or second best when comparing the average RMSE values over the load steps. Out of the five methods, it performed best for 0-percent and 10-percent DLL for both fibers 3 and 4. Since the constant (pre-determined) "c" data was evaluated at a check load of 10-percent DLL and the method performed best at load steps closest to its evaluation point, it leads one to question whether the neutral axis is shifting under wing deformation. By plotting the "c" values of fibers 3 and 4 for 10-percent DLL, -97-percent DLL, and 100-percent DLL (the two extreme load cases), it was clear, at least over the most inboard half of the wingspan, that the neutral axis slightly shifts under load and the "c" values at the 10-percent DLL are bounded by the "c" values of the extreme load cases. Figure 26 shows a shift in "c" values over a portion of the wingspan. Using "c" value data and wing cross-sectional thicknesses at strain stations that cover more than half the wing, the largest average range in "c" values, when considering fiber 3 and 4 separately, covered 5.9 percent of the distance between the respective upper and lower fibers.

Conclusions for this Comparison Study – Table 3 shows a summary of the performance of each method by combining the data from fibers 3 and 4. The last two methods, which use a curve-fit on the real-time "c" values, had mixed results. The curve-fit did not show improvement on the Discontinuous Slope Filter method but it showed improvement on the Discontinuous C Filter method, which also performed the best overall (ranked #1 in table 3). However, unless one can guarantee that the curve-fit will not cross through zero, it may be problematic to use a method that fits a curve in real-time.

Therefore, based on this study, the Check Load method has many merits; however, there are indications that it may not perform as well as the Discontinuous Slope Filter and the Discontinuous C Filter methods over the wing's entire range of motion. This will become more obvious in the example problem in the next section. This disadvantage of the Check Load method may only be due to the properties of the wing that is being considered here. Thus, the Check Load method should still be considered as a method for eliminating discontinuities. For this work though, the Discontinuous Slope Filter and the Discontinuous C Filter methods are recommended as best for calculating displacement over the wing's entire range of motion.

An Example Problem Using the Proposed Methods

In this example, the two recommended methods from the previous section are applied to the same data sets used in the "Wing Bending and Twist Results" section, which showed the calculated displacements and rotations using no filtering method. Six-inch Δl s were used for the shape calculation, as was also used in this example problem for consistency. The purpose of this example is to verify that the recommended methods eliminate the discontinuities that appear near the wing tips in figures 16 and 17, and also that the methods do not create larger errors than those seen using the non-filtered data. Since the focus is only on relative increases or decreases in error, it is sufficient to show the errors in only inches, not percentages, since the percentages become hard to visualize near 0-percent DLL. Figures 27 and 28 show the results for the displacement and twist calculations, respectively. In both figures, the results for the Discontinuous Slope Filter method is shown in the first column with the Discontinuous C Filter method in the second column. For comparison purposes, the results of the Check Load method are also provided for reference at the end of this section and are briefly described.

12

Displacement Results – In figure 27 (a) and (b), improvements are both shown at 0-percent DLL using the two methods. The Discontinuous Slope Filter in figure 27 (a) follows very closely with the calculations of the non-filtered data, while the Discontinuous C Filter in figure 27 (b) usually decreases the error by a small amount, except at 90-percent DLL.

In figure 27 (c) and (d), the errors are slightly larger for the filtered data at 0-percent DLL. The Discontinuous Slope Filter in figure 27 (c) follows very closely with the calculations of the non-filtered data, while the Discontinuous C Filter in figure 27 (d) slightly decreases the error, except at 70-percent DLL.

In figure 27 (e) and (f), both filters eliminate the errors due to discontinuities shown in figure 16 at 60-percent DLL for fiber 3 and figure 17 at 40- and 50-percent DLL for fiber 4. This is encouraging since eliminating discontinuities is the primary purpose of these methods. In one case, the Discontinuous Slope Filter in figure 27 (e) causes more error at 40-percent DLL than the non-filtered data. Further investigation showed that this filtering method actually caused a slight discontinuity in the displacement calculation, where originally there was not one. Appendix A describes how this occurred and offers an improvement to the method, resulting in the Improved Discontinuous Slope Filter method.

Twist Results – Figure 28 (a)-(d) shows that the wing twist calculations for the non-filtered and filtered data are generally the same, with the Discontinuous C Filter method having a slightly worse performance compared to the Discontinuous Slope Filter method. In figure 28 (e) and (f), the peaks in the unfiltered wing twist data are due to discontinuities in the displacement results. The filters clearly remove the peaks from the data. Overall, the improvements using the filtering methods do not minimize the errors in wing twist enough to make the current method for calculating twist a sufficient one.

Check Load Method for Comparison – Figure 29 (a)-(f) shows the results of the Check Load method used for this same example problem. The left hand column shows the displacement results, and the right hand column shows the twist results. In general, the errors due to the Check Load method gradually become larger compared to the unfiltered results as the load increases/decreases away from the 10-percent DLL, the load condition where the "c" data was acquired. However, the method does eliminate the peaks due to discontinuities in the unfiltered results in figure 29 (e), and the maximum absolute wing tip displacement errors are still within 4 in., where the maximum displacement at this span location was 155 in. (13 ft). These small changes in error; however, affect the wing twist calculation, which had absolute errors as large as 14°.

Conclusions and Recommendations for Handling Empirical Data

When using empirical data, several numerical anomalies can disrupt the displacement calculations. The first of the two anomalies discussed in this section was the perfect-zero anomaly. This was successfully addressed by modifying problematic "c" values due to these perfect-zero strains.

The second of the two anomalies was referred to as the C-anomaly. Various methods were proposed and investigated to detect and eliminate the occurrence of larger errors in the displacement calculation due to discontinuities appearing in the calculation (fig. 25). Of these methods, the Check Load method performed very well at load steps near 10-percent DLL, which was the load step used for the check load. The method's performance typically decreased for loads of larger magnitude. This may be due to the properties of the wing structure used for this test, since a comparison of calculated "c" values over the wing's range of motion showed a slight shift in the wing's neutral axis. Even with a performance decrease at extreme load cases, this method may still be good enough for the application at hand when only used for the bending calculations. This method may be very effective for stiffer wings or wings with different

materials or construction. The Global Observer's wing design is proprietary, so our conclusions here remain limited.

Based on the study that compared the five methods using various strain station spacing and the subsequent example problem, the Discontinuous Slope Filter and the Discontinuous C Filter methods are recommended for making the displacement equation more robust to empirical data. Both methods performed very well in eliminating the discontinuities in the displacement calculations. A modification to the Discontinuous Slope Filter method was recommended, resulting in the Improved Discontinuous Slope Filter method; however, even without this improvement, the method had similar performance as the Discontinuous C Filter method in the comparison study using various Δl s.

To this point, effective methods have been developed but none are flawless. The largest area of concern for the two recommended methods is the elimination of strain stations. However, the following three observations have been made:

1. In all example problems throughout this study, it was not found that larger errors were due to too many strain stations being eliminated. The anomalies causing discontinuities were clearly discrete when observing plots of either the slope or "c" values versus the wingspan. This means that unless the chosen tolerance aggressively eliminates non-problematic strain stations, there should be a sufficient amount of remaining data available to do an accurate calculation after elimination. The tolerance levels provided in this study are all based on relative changes in slope or "c" data along the wingspan, making the tolerance levels more applicable to any test structure, especially when strain station spacing is fairly uniform before elimination, as was done here. Between the two methods, there were times when the Discontinuous Slope Filter method eliminated more strain stations than the Discontinuous C Filter method, and vice versa. Eliminating more strain stations did not always correlate with better results. Until the improvement was made to the Discontinuous Slope Filter method, it quite frequently removed non-problematic discontinuities (or strain stations) which did not induce more error, except for the 40-percent DLL case in figure 27 (e).

2. There was no evidence that more consistent spacing of strain stations produced more accurate results. For example, figure 30 shows the calculated displacement at 0-percent DLL using 1-in. Δl 's for three different methods. The Discontinuous C Filter method eliminated 13.55 percent of the strain stations and had a 0.09-in. error. The Discontinuous Slope Filter method eliminated 51.61 percent of the strain stations and had a 0.11-in. error. The Improved Discontinuous Slope Filter method eliminated 21.94 percent of the strain stations and had a 0.06-in. error. The three methods all had the same accuracy in wing tip error; however, they all eliminated a different amount of strain stations. The non-uniformity between the remaining stations, shown in figure 30, did not create more error in the results.

3. In only one instance did the elimination of strain stations cause a new discontinuity between strain stations that originally were not adjacent to one another. This occurred when gathering data for the next section, the sensitivity analysis. Artificial noise was added to all the strains causing two large "c" values adjacent to each other. This was not detectable with the Discontinuous C Filter, the Discontinuous Slope Filter, or the Improved Discontinuous Slope Filter methods. By using the Discontinuous Slope Filter method a second time (two iterations total), the discontinuity was eliminated and the refined results were included in this analysis. In this particular case, more iterations would have helped and addressed the respective concern. However, multiple iterations

14

have also been found to decrease the accuracy of results. For more information on iteration usage, see Appendix A.

Finally, it is recommended that other numerical methods be considered, such as using splines instead of polynomial curve-fits and using median filters. Median filters were partially addressed in this work. Appendix A describes the various issues identified while implementing the median filters. Further work may overcome these issues.

Sensitivity Analysis

Several sensitivity analyses using various inputs to the displacement equation are covered in this section. The Discontinuous Slope Filter method (without the improvement recommended in the previous section) was used to process the data in this section. This method is sufficient for the sensitivity analyses since the results of this section are first reviewed for trends, making errors from discontinuities (if they occur) apparent. For the work provided here, a discontinuity was detected once, and subsequently eliminated by executing a second iteration of the Discontinuous Slope Filter method.

The following subsections will consider the changes in the displacement calculation due to:
1. Noise in the strain data.
2. The distance between strain stations (Δl).
3. The spanwise location of fibers on the wing.
4. The accuracy of the wing's cross-sectional thickness (h).
5. Assumptions at strain station zero.

The "Conclusions and Recommendations" section for this paper will provide a brief summary of all the results of this section.

Noise in the Strain Data

To conduct a sensitivity analysis with respect to noise, the noise range in the FBGs was first determined, along with the noise range of the strain gages for comparison. The span locations chosen for this study were dependent on the locations of the strain gages, since they were not as densely distributed as the FBGs. Four span stations on fiber 3 were chosen at 25-, 51-, 70-, and 88-percent wingspan. The locations of both the strain gages and the FBGs had a few inches of uncertainty in their spanwise location along the wing's 87.5-ft half-span; therefore, the FBG estimated closest to each of the four strain gages was used for comparison purposes. The total range in measurements (that is, max microstrain – min microstrain) was calculated over approximately 20-s intervals for each of the load steps in the positive (increasing load) test case. The time intervals of the two sensors were synchronized as close as possible by matching their respective strain profiles over the entire test.

Figure 31 shows the average noise range and standard deviation of the sensors at the four spanwise locations. This data is plotted for each of the load steps from 0-100 percent positive DLL. The strain gage average noise range is within 5.2 microstrain over all the load steps, where the largest range detected was 7.9 microstrain. On average, the standard deviation was 21 percent of the range. The FBG average noise range was within 16.6 microstrain over all the load steps, where the largest range detected was 18 microstrain. On average, the standard deviation was 28 percent of the range. Strain gage noise slightly increases with higher loads, while the FBGs improve greatly with higher loads, such that their average noise range almost matches that of the strain gages near 100-percent DLL. The decreasing trend seen between the FBG noise range and the percent DLLs is likely due to multiple sources of system noise; the primary source being polarization induced fading (ref 12). The FOSS system used in this testing included

polarization compensation, but the compensation method is not yet perfect. Polarization induced fading, along with other noise sources, is continuously being mitigated through FOSS system development.

The second part of this study is to determine the sensitivity of the displacement calculations to the noise ranges calculated above, where the largest detected range was 18 microstrain, occurring at 0-percent DLL. This range of 18 microstrain could also be considered as ±9 microstrain, but as an absolute worst case, this study includes the ±18 microstrain in every strain value along the wing's four fibers. A 6-in. Δl was used for all for displacement calculations for each of the following four load steps: -97-percent DLL (-1 g), 0-percent DLL (0 g), 10-percent DLL (0.3 g), and 100-percent DLL (3 g). Five test cases were performed as follows:

1. All fibers: no artificial strain included.
2. All fibers: +18 microstrain.
3. All fibers: -18 microstrain.
4. Top surface fibers: +18 microstrain, bottom surface fibers: -18 microstrain.
5. Top surface fibers: -18 microstrain, bottom surface fibers: +18 microstrain.

Figures 32 and 33 show the displacement calculations for fibers 3 and 4, respectively. When looking at the displacement errors in inches, a clear trend is detected. Case 2 and 3 do not have much of an effect on the displacement calculation when compared to case 1, the calculation when no artificial noise was added. This is likely due to the artificial noise being canceled out (eliminated) in the denominator of the "c" value equations (eq. (4)), since the same strain was added to both the top and bottom fibers which does not change the difference between the fibers' strain values. However, cases 4 and 5 are indeed affected by the artificial noise. In case 4, the artificial noise makes the difference in the denominator of the "c" value smaller. This makes the resulting "c" value larger, meaning that the wing is falsely stiffened. Thus, the result is an under-prediction when compared to case 1 (no addition of artificial noise). The exact opposite is true for case 5. For case 4, the approximate offset for fiber 3 is -1.25 in. and for fiber 4, -2.75 in. For case 5, the approximate offset for fiber 3 is 1.5 in. and for fiber 4, 2.25 in. The differences in offsets between the forward and aft fibers, suggests that system noise may indirectly cause slight wing twist errors.

Figure 32 and figure 33 clearly show an error band due to noise that is bounded by case 4 and case 5. However, this error band is overly-conservative for two reasons: (1) the entire noise range (18 microstrain) was artificially added in both directions (essentially creating a noise range of 36 microstrain) and (2) the worst case noise range was added over every load step, when other load steps did not see this high of noise levels. It is encouraging that the error band for both fibers almost completely contains the zero error line, which corresponds to the actual displacement measured by the photogrammetry.

These results suggest that noise in the strain values affects the displacement calculations, but only within ±2.75 in., which is quite good considering the wing's 87.5-ft half-span.

Distance Between Strain Stations (Δl)

To conduct a sensitivity analysis with respect to the distance between strain stations (Δl), the displacement calculations were performed for -97-, 10-, and 100-percent DLL using various values for Δl's, ranging from 1 to 492 in. shown in table 4. The sensing length of 959 in. is defined here as the distance between the first and the last strain station, where the last station chosen for this analysis aligns directly with a photogrammetry station. Previously, only relatively small Δls (1-12 in.) were used, such that if one of their span stations did not coincide directly with the photogrammety station used for the wing tip measurement, the calculated displacement was simply interpolated at the location of the

16

photogrammetry station for comparison. With the use of larger Δl s, errors from interpolation may become significant.

Two spanwise gaps in each fiber length occur at the wing joints, such that no strain stations are located in these regions. This explains why the number of strain stations for the 1 inch Δl is less than 959 in. The largest Δl, 41 ft has only three strain stations (one near the centerline, midspan, and tip).

Figure 34 to figure 36 shows the displacement errors for fibers 3 and 4, at -97-, 10-, and 100-percent DLL respectively, for each of the Δl s in table 4. There is no clear correlation between the size of the Δl s and the displacement error, except that the errors are generally smaller for smaller Δl s and larger for larger Δl s. When comparing the results between -97-, 10-, and 100-percent DLL (while recalling that an under-prediction for the -97-percent DLL case is a positive number, whereas an under-prediction for the 10- and 100-percent DLL cases is a negative number), the results using 12 and 16-ft Δl s typically underpredict the displacement whereas the results using 20-, 27-, and 41-ft Δl s typically overpredict the displacement. At this point, there is no definitive explanation for this.

To determine the general consistency (or increase) in displacement error for -97-, 10-, and 100-percent DLL, figure 37 shows the change in the absolute maximum error between fibers 3 and 4, where the values are normalized to the largest absolute error detected. These plots essentially bound the error, and only increase in their value when a larger absolute error occurs. From the data, the errors for each of the three load steps are fairly well bounded at 1-ft Δl s (approximately 1.25 percent of the total sensing length) and smaller. These normalized errors at 1-ft Δl s and lower correspond to the errors shown in table 5 where the error in inches is bounded by ±3.16 in. (-97-percent DLL) and for percents, ±7.53 percent (10-percent DLL).

Finally, the data was reviewed to determine whether there is a particular Δl that has the best performance. The errors for fibers 3 and 4 were combined into a single error value, using their RMSE. Then, for each Δl, the average RMSE value for the 3 load steps considered was plotted in figure 38. The RMSE values have a fairly consistent trend for 1 in. to 4 ft, compared to the Δl s larger than 4 ft. Between 1 in. and 4 ft, the Δl s at 6 and 12 in. had the best performance. This may suggest that spacing near 0.63 to 1.25 percent of the sensing length are optimal. To confirm this hypothesis, Δl sensitivity analyses would have to be conducted on test articles of different scales other than the Global Observer.

Spanwise Location of Fibers on the Wing

Each of the four spanwise fibers is made up of 3 individual fibers with 2 gaps in between them, as shown in figure 5. Therefore, a total of 12 fibers are installed on the wing. Prior to ground load testing, the location of the start and end points of these fibers were recorded. The first and last FBG number on each of the 12 spans was also recorded. After the testing, the strain data was also reviewed for consistency with the recorded fiber locations. However, in determining the exact location of an individual FBG along the wing's 87.5-ft half-span, there is still some uncertainty, on the order of a few inches. Therefore, this study investigates the affect of changing the spanwise locations of the FBGs.

Twelve cases were executed, one for each of the 12 individual fibers on the wing, beginning with fiber 1 and the most inboard fiber, and proceeding to the outboard fibers consecutively. Then fiber 2 was investigated, from inboard to outboard, and so on. To modify the FBG locations for each of the 12 individual fibers, each FBG strain was changed to the 6th previous FBG strain reading. This essentially shifts the FBG readings 3 in. outboard (since the FBGs are spaced approximately 0.5 in. apart). With this shift, the inboard FBGs for each fiber may be pulling strain readings from parts of the fiber that were not fixed to the wing, potentially adding some error. At the outboard end of the fiber, the last 6 strain readings

on the fiber are not used. Since the strains are generally higher toward the wing's centerline, this indirectly creates higher strains on individual fibers.

After running all 12 test cases, one for each fiber, the displacement calculations for fibers 3 and 4 covered the range of displacements shown in table 6. The variances either made the calculations more accurate or less accurate. Overall, the greatest range in displacement calculations in inches was 1.82 in. at -97-percent DLL and for percents, 4.83 percent at 10-percent DLL. Therefore, the accuracy of the location of the fibers could be affecting the displacement results, but considering the wing's 87.5-ft half-span, the results are fairly insensitive to shifts in FBG locations.

Accuracy of the Wing's Cross-sectional Thickness (h)

The accuracy of the wing's cross-sectional thickness affects the parameter "h" (the distance between corresponding top and bottom fibers) in the "c" equation (eq. (4)). Since the wing geometry used for this study was based on modeled geometry and not the actual fabricated geometry, the goal of this section is to determine the sensitivity of the displacement results to "h." Load steps -97-, 10-, and 100-percent DLL were chosen for this study, and a 6-in. Δl was used for each displacement calculation. The "h" values over the entire wingspan were modified 4 times, using the following percent changes on "h": -10, -5, 5, and 10 percent. In the displacement equation, this modification of the "h" value does not affect the c-ratio values since the modification factors cancel out between the numerator and the denominator.

When modifying the "h" values by -10, -5, 5, and 10 percent, the results proved to be fairly linear, such that the following results are summarized by 1-percent changes in wing thickness. For a 1-percent increase in thickness, the wing becomes stiffer and results in a 0.85-percent decrease in displacement compared to the results when the "h" value is not modified. This 0.85-percent decrease is approximately the following in inches: 0.39 in. for the -97-percent DLL, 0.13 in. for the 10-percent DLL, and 1.30 in. for the 100-percent DLL. For a 1-percent decrease in thickness, the wing becomes less stiff and results in a 0.95-percent increase in displacement, which is approximately the following in inches: 0.41 in. for the -97-percent DLL, 0.15 in. for the 10-percent DLL, and 1.50 in. for the 100-percent DLL. Overall, it can be estimated that a 1-percent change in thickness causes a 1-percent change in wing tip displacement. Once again, low sensitivity is encouraging.

Assumptions at the First Strain Station

As explained in the "Ground Loads Testing Using FOSS" section, the first strain station could not be located at the wing's centerline, so it was located 65.77 in. outboard the centerline. The displacement and slope at the first strain station are inputs to the displacement equation (eq. (1)) and were calculated using the photogrammetry data. Normally, the first strain station is at the root of the wing, such that the displacement and slope is always zero. At 65.77 in. outboard of the centerline, the displacements and slopes were relatively small (the largest being 0.5-in. and 0.8°). This study looks at the sensitivity of the displacement calculations if these displacement and slope values were assumed to be zero.

Table 7 shows that the assumption of zero displacement and slope at 65.77-in. span causes an under-prediction of the results achieved when the actual displacement and slopes are implemented, for the three load steps considered (-97-, 10-, and 100-percent DLL). The RMSE of these under-predictions is 8.54 in. or 9.66 percent. Table 7 also shows that in only one instance did this under-prediction decrease the error. It occurred with fiber 4 at 10-percent DLL, which originally over-predicted the actual by 0.90 in. With the assumption of an initial zero displacement and slope, the results were an under-prediction of the actual by 0.5 in., making a small improvement in the absolute error. In all other cases though, the smaller calculated

18

displacements increased the absolute error. These values are noted as negative values in last 2 columns of table 7.

Conclusions and Recommendations

This paper explored the accuracy of wing shape calculations of a full-scale structure over its entire range of motion, using empirical data from fiber optic strain measurements. Prior to this test, the deformed shape equations had only been verified using strain data from a finite element analysis model and minimal (small loads and displacements) experimental testing. The results are as follows:

1. Across the wingspan, the strain measurements of the FBGs compared extremely well with those of the strain gages.
2. Initial results using the deformed shape equations were in excellent agreement with the actual tip deflections for wing bending. The results, measured at a span location of 1025 in. from the centerline, were within ±2.7 in. (out of 115-in. (13-ft) max deflection) for 91 percent of the load steps. This experimental testing revealed valuable opportunities for improving the deformed shape equations' robustness to real world (not perfect) strain data, which previous analytical testing did not detect. These improvements minimize errors due to numerical anomalies that were discovered in the remaining 9 percent of the load steps, enabling all load steps to attain accuracy within ±2.7 in.
3. Results for the wing twist were found to be very sensitive to errors in bending and require further development. It may prove helpful to acquire off-axis, not only unidirectional (that is, spanwise), strain data.

A sensitivity analysis revealed the following about the application of wing shape calculation algorithms to this 175-ft span structure:

1. An overly-conservative noise sensitivity analysis showed an error band within ±2.75 in. of the calculated wing tip displacement, with the zero-error line being almost completely enclosed by this band.
2. Displacement calculations using Δl s greater than 4 ft showed larger or less consistent errors compared to those using smaller Δl s. At Δl s of 4 ft or smaller, the best two Δl values were 6 in. (0.63 percent of the sensing length) and 12 in. (1.25 percent of the sensing length).
3. Shifting each of the 12 individual fibers 3 in. outboard, one at a time, created a maximum range of wing tip displacement calculations that covered 1.82 in. at -97-percent DLL (when considering inches) and 4.83 percent at 10-percent DLL (when considering percents).
4. A 1-percent change in cross-sectional thickness between upper and lower fibers causes a slightly less than 1-percent change in the wing tip's displacement. If the cross-sectional thickness becomes larger, the wing tip displacement becomes smaller, and vice-versa.
5. If the actual displacement and slope of the first strain station, which was not located at the wing's centerline, were assumed to be zero, this would have changed the displacement results by 8.54 in. or 9.66 percent, using RMSE values. In all cases, these changes in displacement cause an under-prediction of the wing tip displacement.

The following recommendations are made for the best placement of fibers along a wing:

1. Locate the first strain station at the wing's root and ensure that accurate strain measurement can be made or extrapolated there. If fibers cannot be installed at or near the root, use strain gages in that location.
2. The following recommendations pose trade-offs with each other; however, the first recommendation should be given the highest priority:
   a. Since numerical anomalies typically occur in regions where the strains are small, install fibers as far away from the neutral axis as possible, since strains at the neutral axis are zero.

b. Since the wing twist measurement is more sensitive to smaller "d" values (the chord-wise distance between the forward and aft fibers), place the fibers as far apart as possible.

The following recommendations are made for achieving the most accurate results using the deformed shape equations:

1. For a test article of this scale, the best Δl values should be 0.63-1.25 percent of the sensing length, requiring the use of FOSS instead of strain gages. When scaled to an 8-ft wing, for example, the Δl s would be every 0.6-1.2 in. Fibers which have continuous gratings (that is, gratings every 1/8 in.) have already been developed and may be very applicable to smaller-spanned structures.

2. Various filtering methods were developed and shown to be effective in minimizing errors due to numerical anomalies. Two methods, the Improved Discontinuous Slope Filter and the Discontinuous C Filter method, were recommended for this application; however, the Check Load method should still be considered for other test articles, since its performance may have been dependent on this particular test article. Further research into other data smoothing techniques, such as splines or median filters, may prove to be valuable.

Potential FOSS and Shape Sensing Capabilities

The FOSS system and shape sensing capabilities are continuously being improved though system updates and new fiber technology including continuous grating fibers and multi-core fibers. Potential future capabilities include:

1. Updates to the FOSS system design that will reduce costs for larger scaled systems, used on transports for example, by enabling the use of a single laser over a larger number of fibers. The system design is also becoming more compact and ruggedized for operation on small unmanned aerial vehicles and more aggressive vehicles.

2. Continuous grating fibers and the development of their processing algorithms should enable a higher density of strain readings (1/8-in. FBG spacing or smaller) for applications that require higher strain resolution.

3. Multi-core fibers are comprised of 3 single fibers arranged 120° apart and have the ability to measure displacement in three dimensions. They do not require physical attachment to a structure to calculate their position in space.

Tables

Table 1. Comparison of wing tip out-of-plane displacement results of fiber 3 when various filtering methods (including no filter) are implemented.

Table 1a. Fiber 3: errors in wing tip displacement using no filter for different Δl values and load steps.

Approximate Delta L, in.	Percent DLL							
	-97	-50	-10	0	10	50	100	
1	3.13	2.03	0.31	0.17	-1.33	-2.59	-2.44	in.
	(-6.70)	(-8.29)	(-6.95)	(-1266.25)	(-8.36)	(-3.30)	(-1.58)	(%)
4	**-9.24**	1.92	0.55	0.08	-1.29	-2.79	-2.67	in.
	(19.79)	(-7.83)	(-12.04)	(-566.41)	(-8.13)	(-3.56)	(-1.72)	(%)
6	1.97	1.30	0.14	1.89	-1.01	-1.02	0.73	in.
	(-4.23)	(-5.33)	(-3.00)	(-14111.41)	(-6.34)	(-1.31)	(0.47)	(%)
12	2.34	1.54	0.53	1.57	**5.45**	-1.62	-0.14	in.
	(-5.01)	(-6.29)	(-11.61)	(-11727.89)	**(34.36)**	(-2.06)	(-0.09)	(%)
RMSE	5.11	1.72	0.42	1.23	2.92	2.13	1.84	in.

Table 1b. RMSE (inches) in wing tip displacement using various filtering methods.

Method	Percent DLL							Average RMSE per row	Ranking
	-97	-50	-10	0	10	50	100		
No filter	5.11	1.72	0.42	1.23	2.92	2.13	1.84	2.20	4
Checkload	<u>1.27</u>	<u>1.28</u>	0.18	<u>0.10</u>	<u>1.08</u>	1.85	1.98	1.11	1
Discontinuous slope	2.65	1.73	0.26	1.51	1.18	2.13	1.84	1.62	3
Discontinuous C	2.39	1.62	0.30	0.33	1.17	1.89	2.68	1.48	2
Curvefit discontinuous slope	2.14	1.48	0.22	147.93	1.10	<u>1.65</u>	<u>0.75</u>	22.18	5
Curvefit discontinuous C	2.24	1.44	<u>0.17</u>	0.23	1.13	1.89	0.79	1.13	1

*Underlined values are the lowest RMSE per load step.

Table 2. Comparison of wing tip out-of-plane displacement results of fiber 4 when various filtering methods (including no filter) are implemented.

Table 2a. Fiber 4: errors in wing tip displacement using no filter for different Δl values and load steps.

Approximate Delta L, in.	Percent DLL							
	-97	-50	-10	0	10	50	100	
1	-0.49	3.08	0.36	-0.32	**2.77**	0.01	2.25	in.
	(1.06)	(-12.64)	(-7.78)	(528.78)	**(17.51)**	(0.01)	(1.45)	(%)
4	2.95	2.67	-0.16	**-17.79**	**4.95**	-0.79	0.39	in.
	(-6.30)	(-10.94)	(3.52)	**(29055.20)**	**(31.33)**	(-1.00)	(0.25)	(%)
6	2.60	3.05	0.56	1.10	0.89	-0.24	0.82	in.
	(-5.57)	(-12.51)	(-12.21)	(-1796.36)	(5.66)	(-0.31)	(0.53)	(%)
12	3.22	2.62	0.47	**4.62**	1.28	-1.06	-0.68	in.
	(-6.89)	(-10.72)	(-10.20)	**(-7537.29)**	(8.11)	(-1.35)	(-0.44)	(%)
RMSE	2.55	2.86	0.41	9.21	2.94	0.67	1.26	in.

Table 2b. RMSE (inches) in wing tip displacement using various filtering methods.

Method	Percent DLL							Average RMSE per row	Ranking
	-97	-50	-10	0	10	50	100		
No filter	<u>2.55</u>	2.86	0.41	9.21	2.94	0.67	1.26	2.85	4
Checkload	4.25	3.20	0.39	<u>0.26</u>	<u>0.59</u>	<u>0.60</u>	3.77	1.87	2
Discontinuous slope	3.03	2.64	<u>0.32</u>	0.76	0.69	0.95	0.95	1.33	1
Discontinuous C	2.95	<u>2.61</u>	<u>0.32</u>	0.45	0.74	1.04	0.94	1.29	1
Curvefit discontinuous slope	3.13	2.68	0.53	0.66	0.61	6.44	1.26	2.19	3
Curvefit discontinuous C	3.44	2.64	0.34	0.37	0.71	1.09	<u>0.74</u>	1.33	1

*Underlined values are the lowest RMSE per load step.

Table 3. A summary of the performance of various filtering methods used for fibers 3 and 4.

Method	Average RMSE for fibers 3 & 4	Ranking	Percent improvement compared to RMSE for no filter	Recommendation
No filter	2.52	5	-	
Check load	1.49	4	35.9%	2nd
Discontinuous slope	1.47	3	36.4%	1st
Discontinuous C	1.39	2	40.2%	1st
Curvefit discontinuous slope	12.18	6	-425.5%	
Curvefit discontinuous C	1.23	1	47.0%	

Table 4. Values used for the Δl sensitivity analysis.

Approximate Δl, in.	Approximate Δl, ft	Percent of sensing length (959 in.)	Number of stations prior to filtering
1	0.08	0.10	913
4	0.33	0.42	230
6	0.50	0.63	153
12	1.00	1.25	78
24	2.00	2.50	39
36	3.00	3.75	27
48	4.00	5.01	20
96	8.00	10.01	11
144	12.00	15.02	8
192	16.00	20.02	6
240	20.00	25.03	5
324	27.00	33.79	4
492	41.00	51.30	3

Table 5. Wing tip out-of-plane displacement errors that correspond to the normalized errors at 1-ft Δl s (and smaller) in figure 37.

Displacement error	-97-percent DLL	10-percent DLL	100-percent DLL
Inches	3.16	1.19	2.44
Percent	(6.76)	(7.53)	(1.58)

Table 6. Results for the sensitivity analysis on the spanwise location of fibers.

Percent DLL	Range in displacement calculations due to modified FBG locations		
	Fiber 3	Fiber 4	
100	0.89	1.79	in.
	(0.58)	(1.15)	(%)
10	0.15	0.76	in.
	(0.95)	(4.83)	(%)
-97	0.25	1.82	in.
	(0.53)	(3.90)	(%)

Table 7. Results for the sensitivity analysis on the displacement and slope measurements assumed at the first strain station.

	Change in displacement calculation: difference in displacement calculation when assuming zero displacement and slope at the first strain station	Change in absolute error: negative values indicate the increase in absolute error by assuming zero displacement and slope at the first strain station		
	Average over fibers 3 and 4	Fiber 3	Fiber 4	
100	-13.68	-12.13	-12.13	in.
	(-8.83)	(-7.83)	(-7.83)	(%)
10	-1.28	-1.16	0.40	in.
	(-8.07)	(-7.33)	(2.51)	(%)
-97	5.47	-5.55	-5.38	in.
	(-11.70)	(-11.89)	(-11.51)	(%)
RMSE over the three load steps	8.54			in.
	(9.66)			(%)

Figures

Figure 1. The Global Observer.
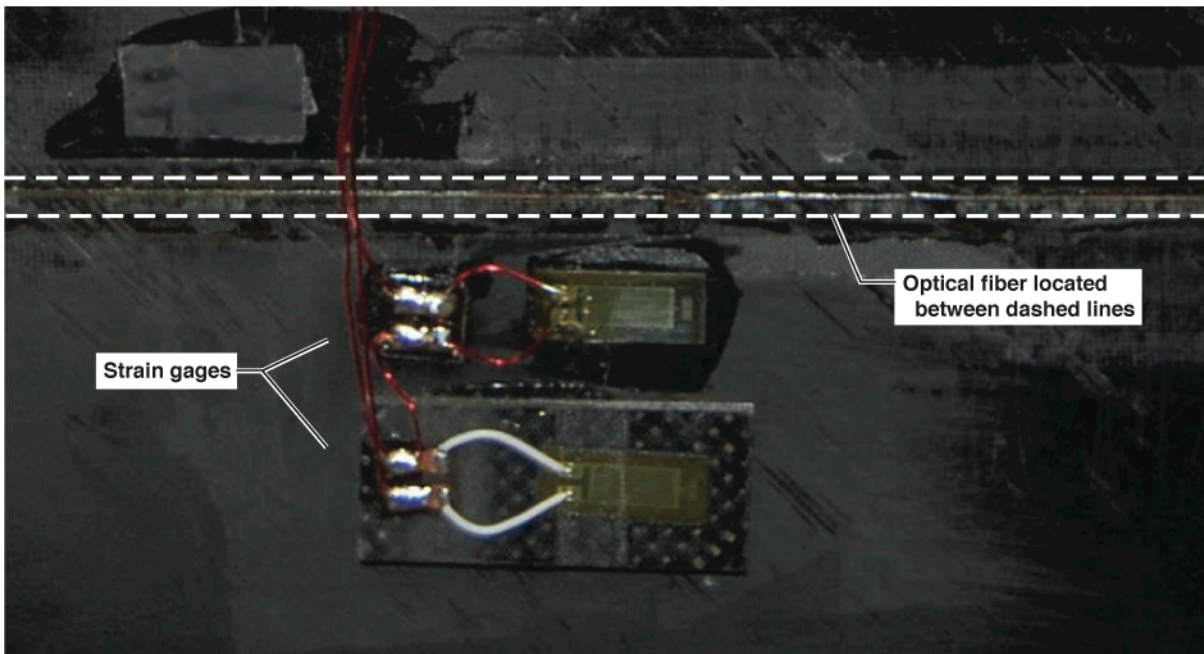
Figure 2. Comparison of strain gages and fiber.
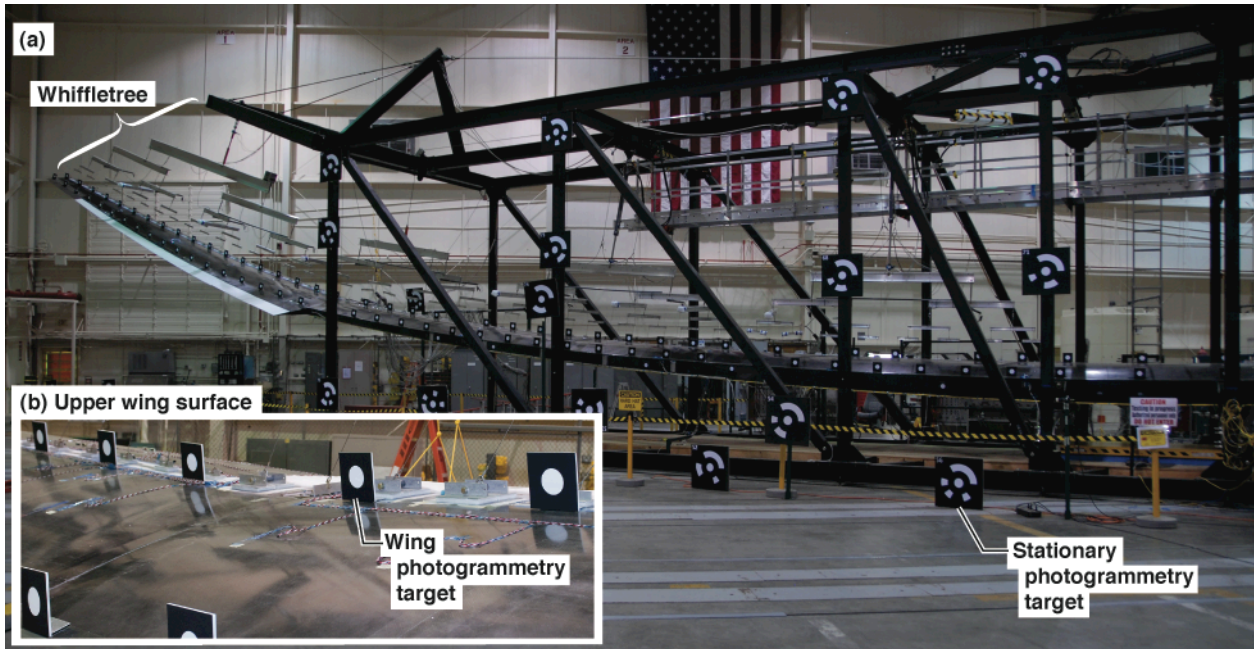
Figure 3. The left wing of the Global Observer deforming under load during ground loads testing in the NASA Dryden Flight Research Center's Flight Loads Laboratory.
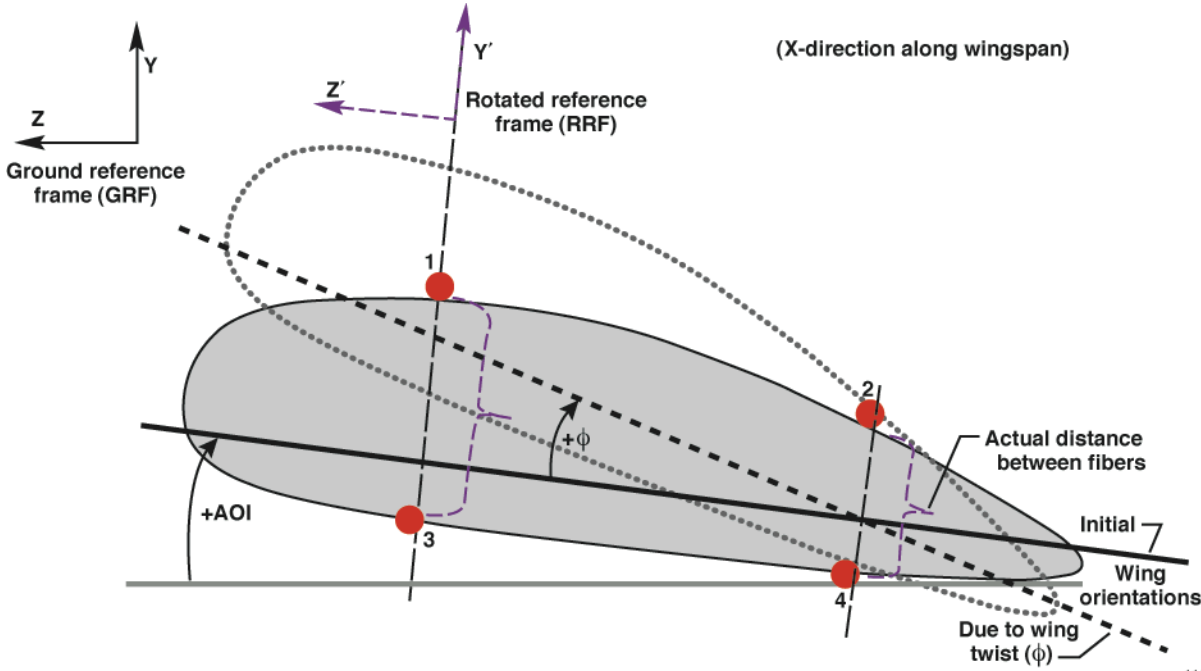
Figure 4. The general location of fibers 1 through 4 on the wing's cross-section, and the coordinate systems used in this work, which were based on consistency with the deformed shape equations (bending and twist).
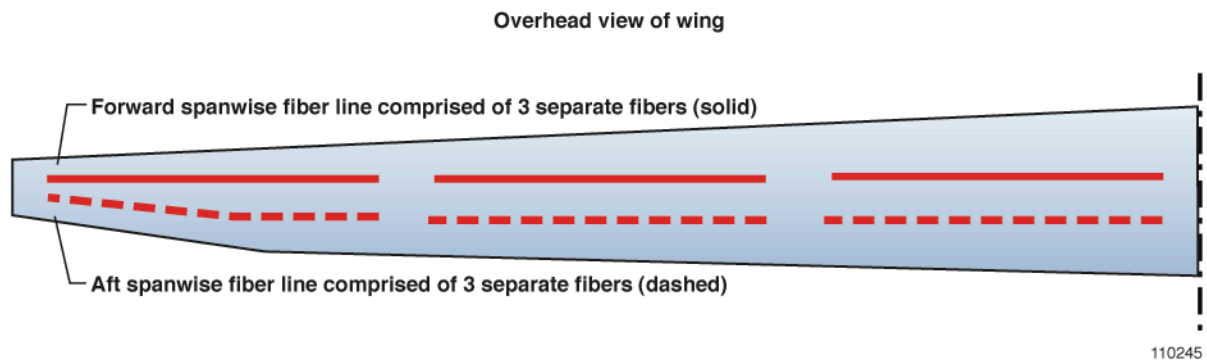
Figure 5. Layout of fibers on the top surface of the wing.
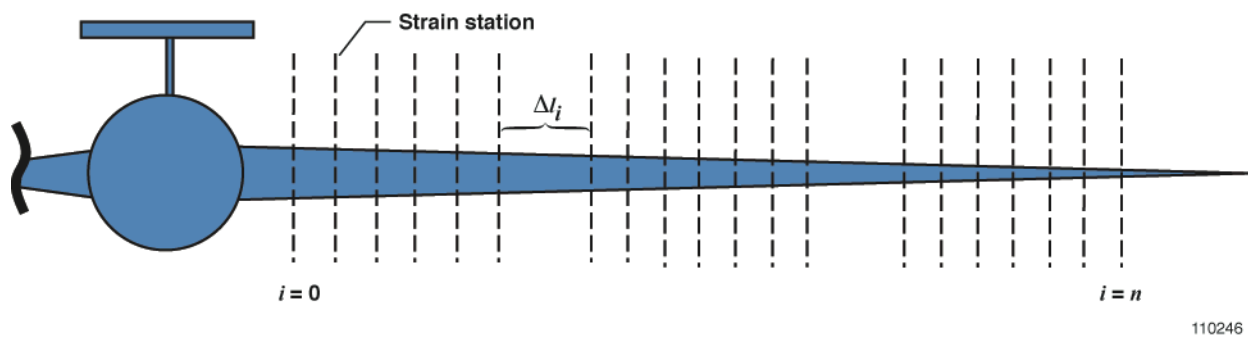
Figure 6. Illustration of the distance between strain stations (Δl).
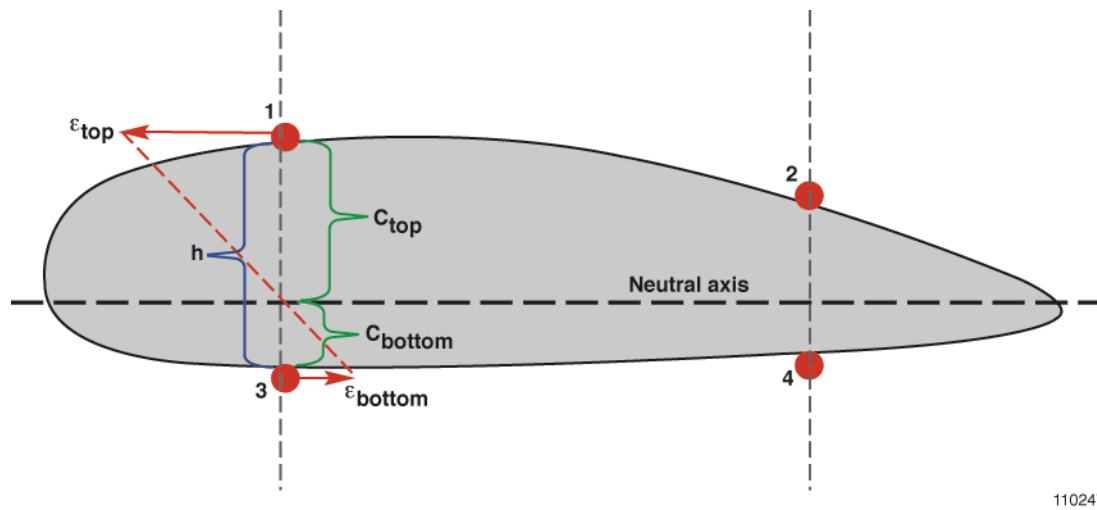
Figure 7. A wing cross-section showing how the neutral axis is determined from the strain measurements.
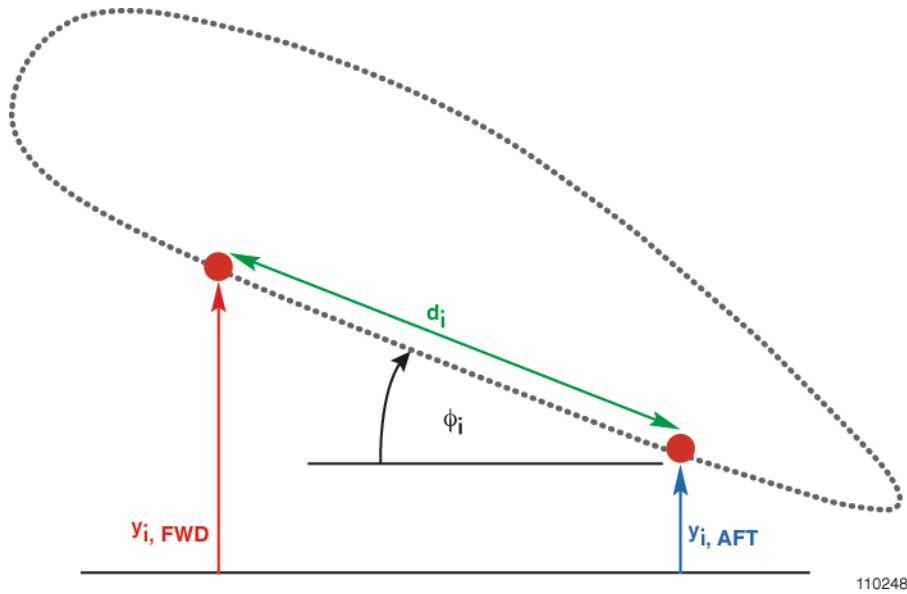
Figure 8. Illustration of the calculation of twist angle (ϕ) from the displacements of the forward and aft fibers.
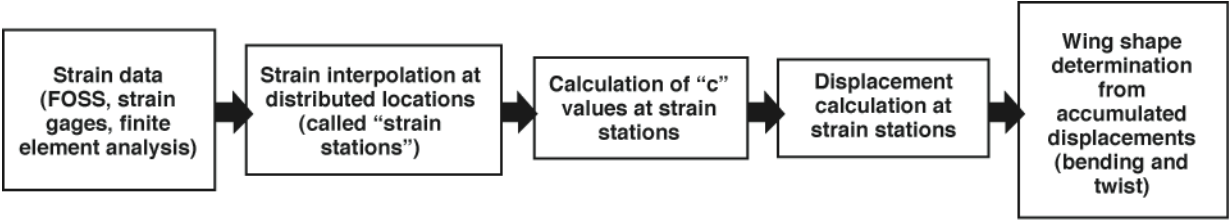
Figure 9. Overview of the deformed wing shape calculation method.

28
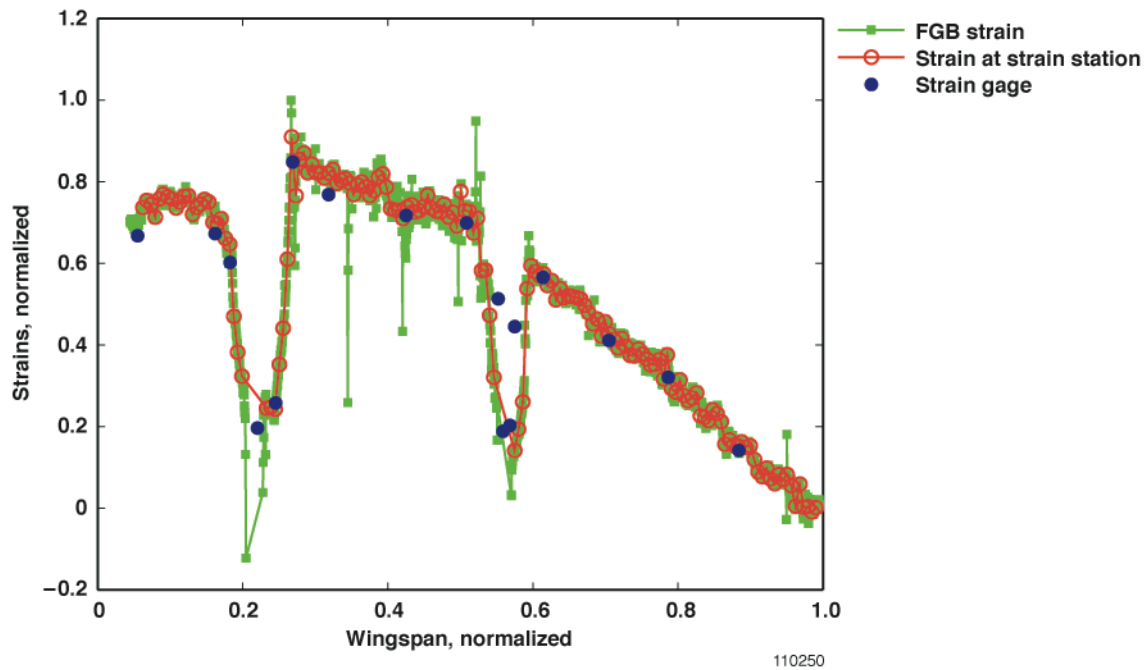
Figure 10. Normalized fiber optic strain data along one of the wing's 4 spanwise fibers, extending from root to tip.
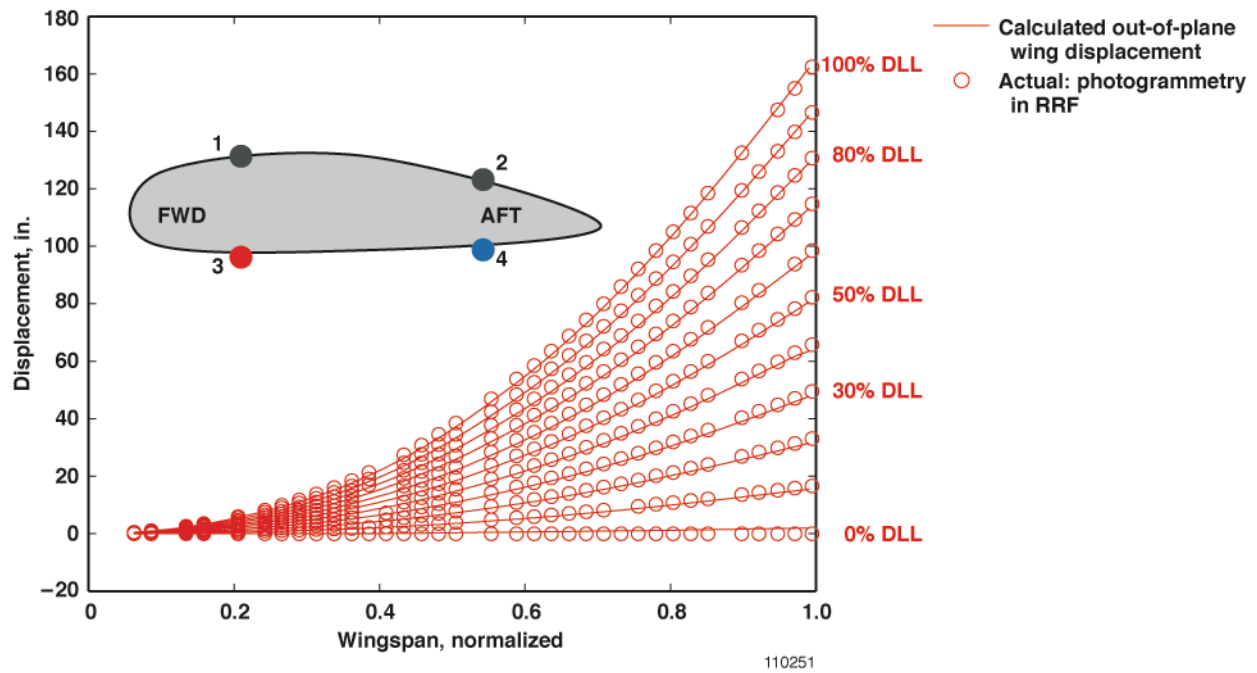
Figure 11. Fiber 3 out-of-plane displacement results while load was increased from 0 to positive 100-percent DLL at 10-percent DLL increments.

29
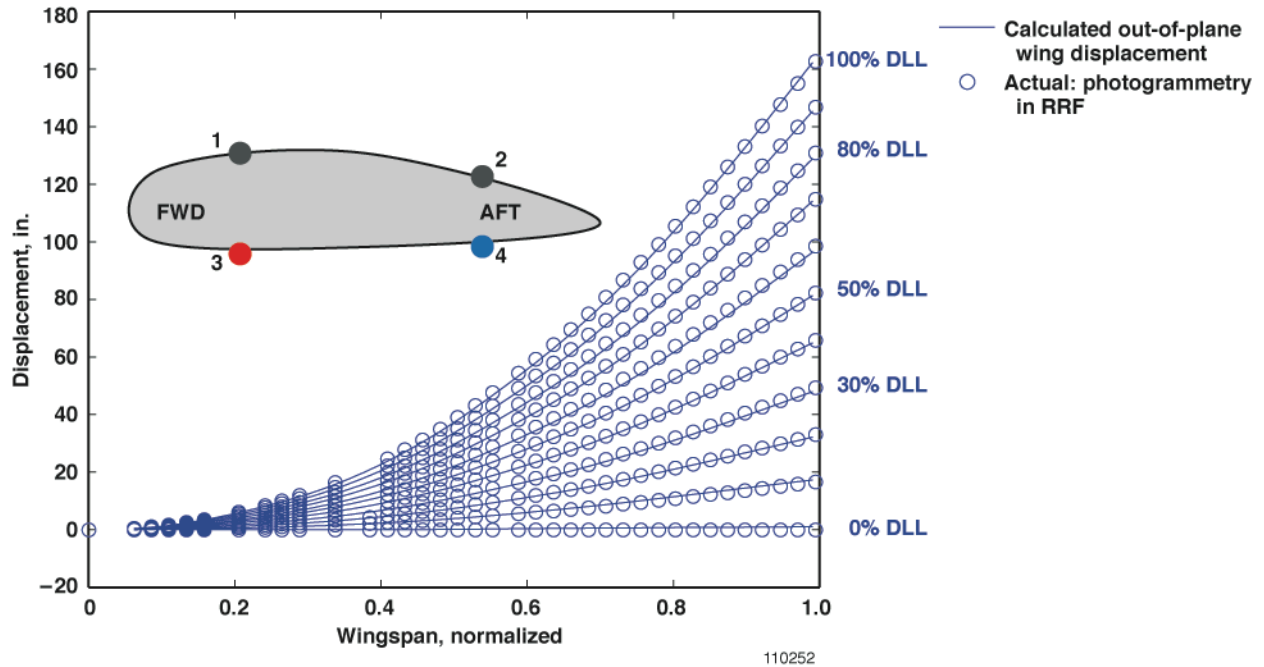
Figure 12. Fiber 4 out-of-plane displacement results while load was increased from 0 to positive 100-percent DLL at 10-percent DLL increments.
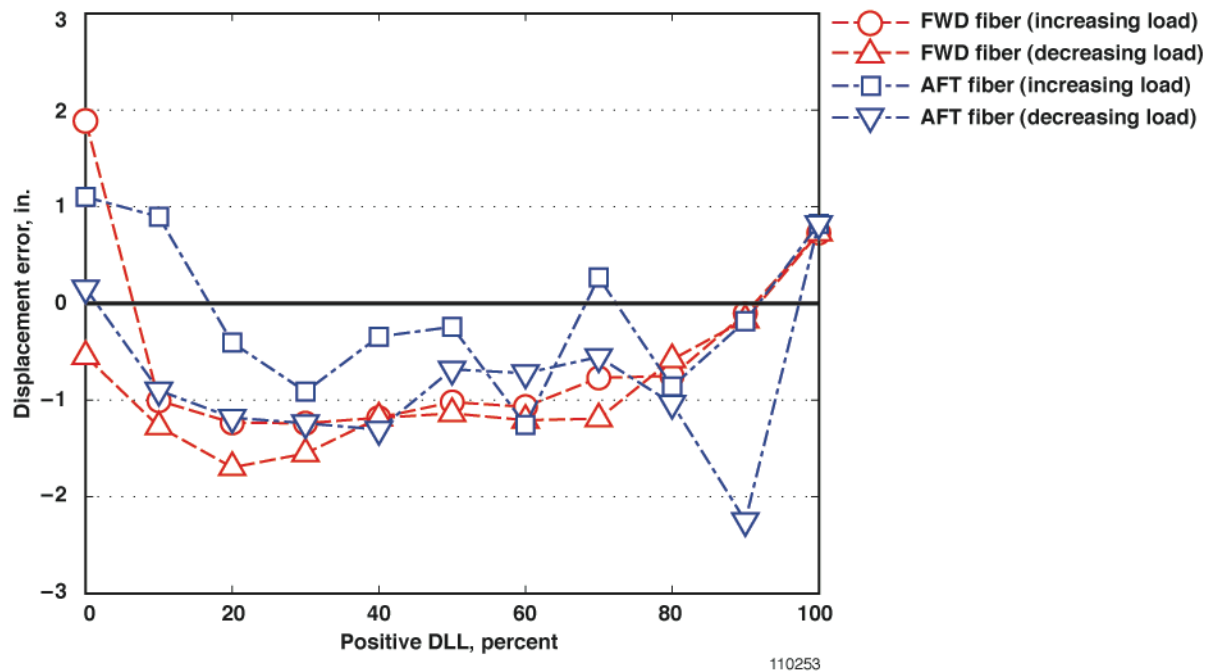
Figure 13. Wing tip out-of-plane displacement error in inches for the span location of 1025 in. (85.4 ft) from the wing centerline for the positive load case.
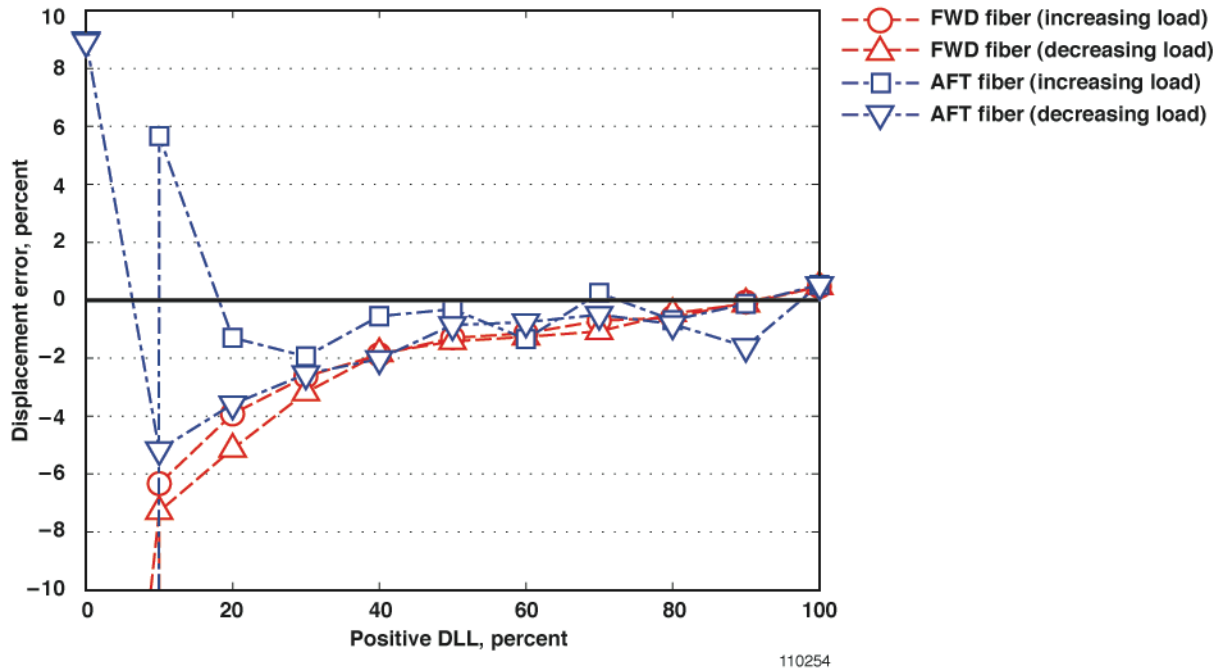
Figure 14. Wing tip out-of-plane displacement error in percent for the span location of 1025 in. (85.4 ft) from the wing centerline for the positive load case.
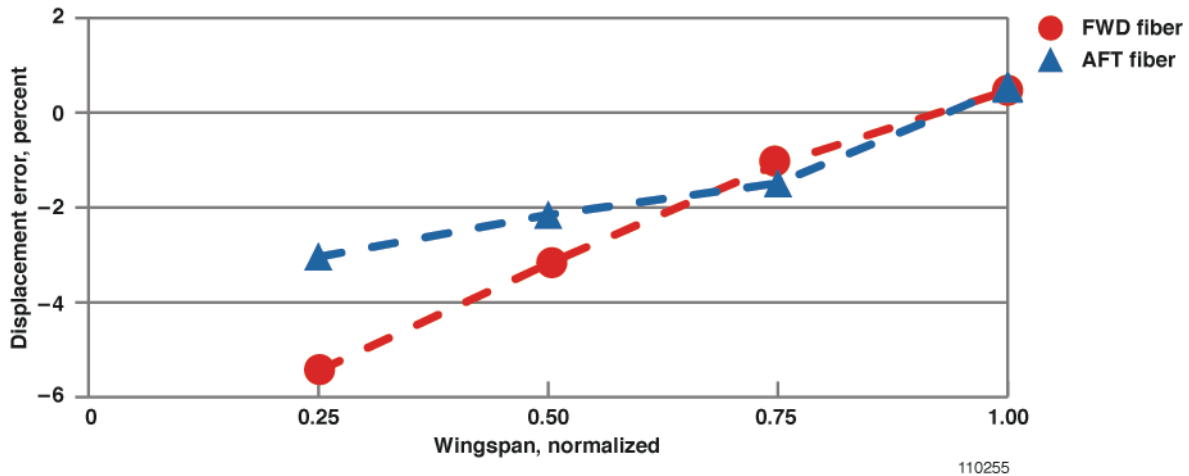
Figure 15. Out-of-plane displacement error in percent near four span stations (25, 50, 75, and 100-percent wingspan) for the positive 100-percent DLL load case.
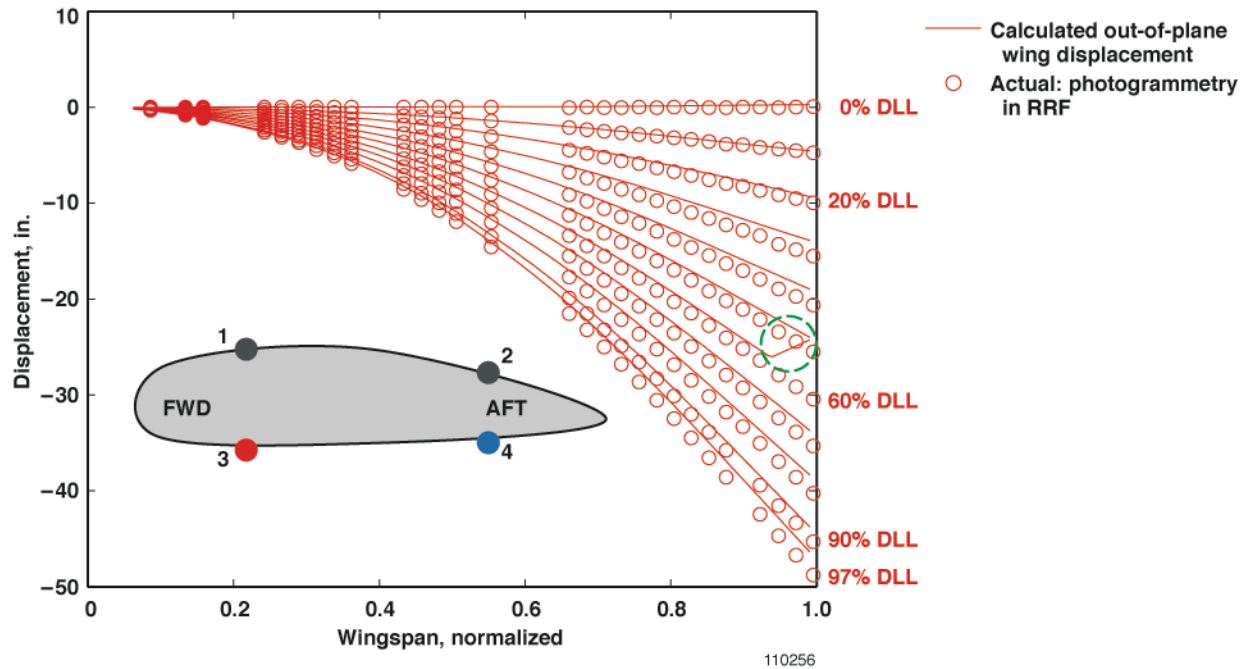
Figure 16. Fiber 3 out-of-plane displacement results while load was increased from 0 to negative 97-percent DLL at 10-percent DLL increments.
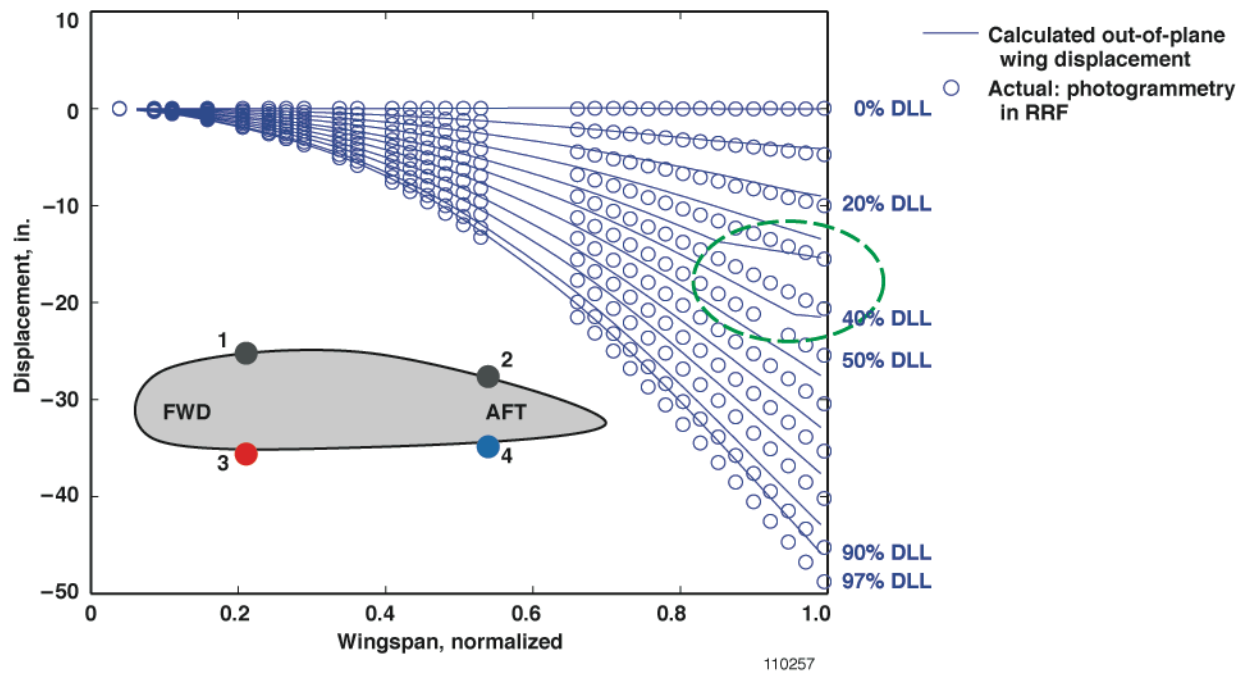
Figure 17. Fiber 4 out-of-plane displacement results while load was increased from 0 to negative 97-percent DLL at 10-percent DLL increments.
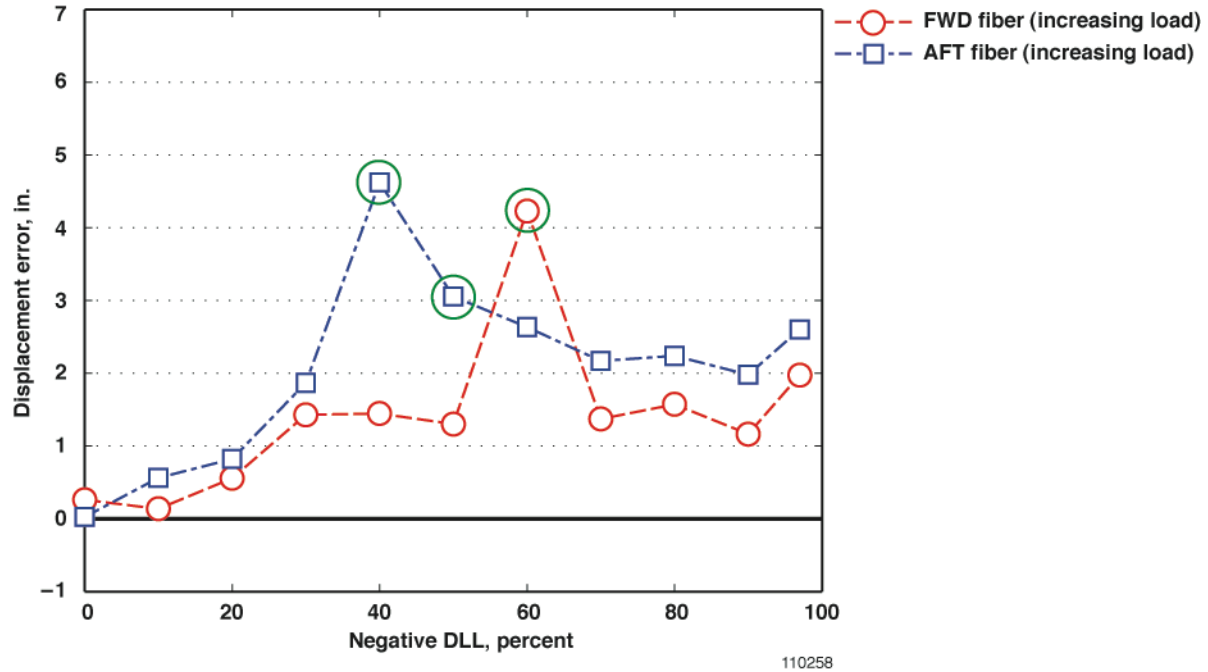
Figure 18. Wing tip out-of-plane displacement error in inches for the span location of 1025 in. (85.4 ft) from the wing centerline for the negative load case. Circled results show where discontinuities appeared in the displacement calculation.
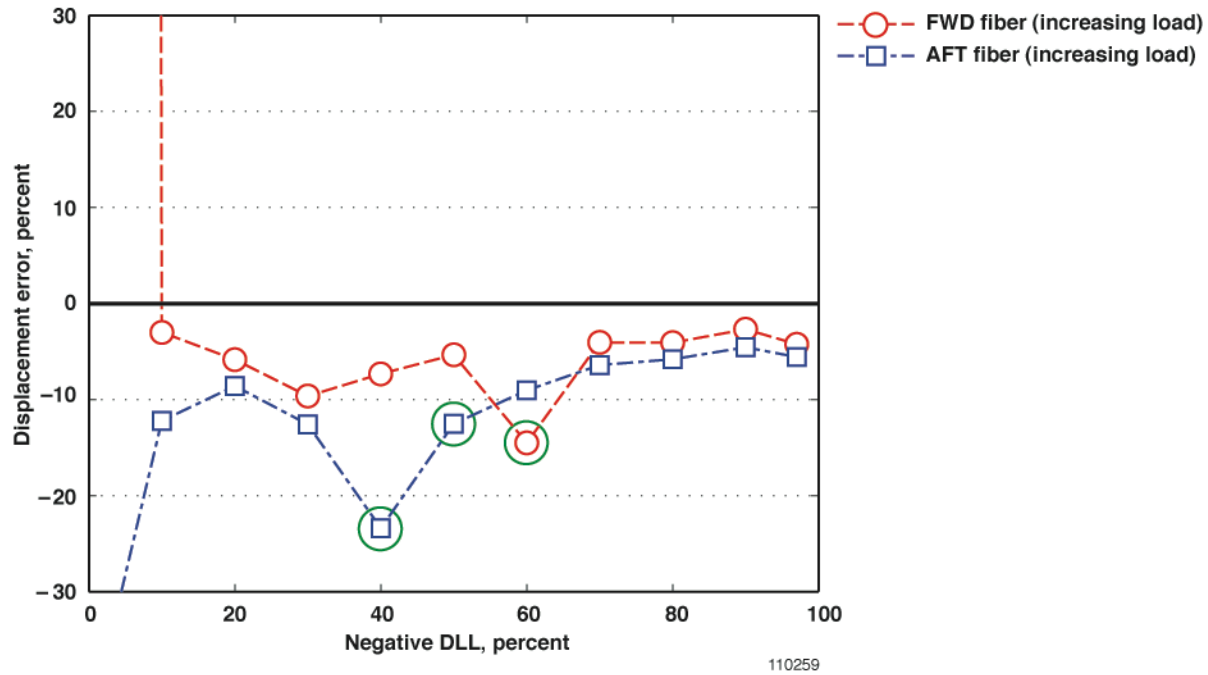
Figure 19. Wing tip out-of-plane displacement error in percent for the span location of 1025 in. (85.4 ft) from the wing centerline for the negative load case. Circled results show where discontinuities appeared in the displacement calculation.
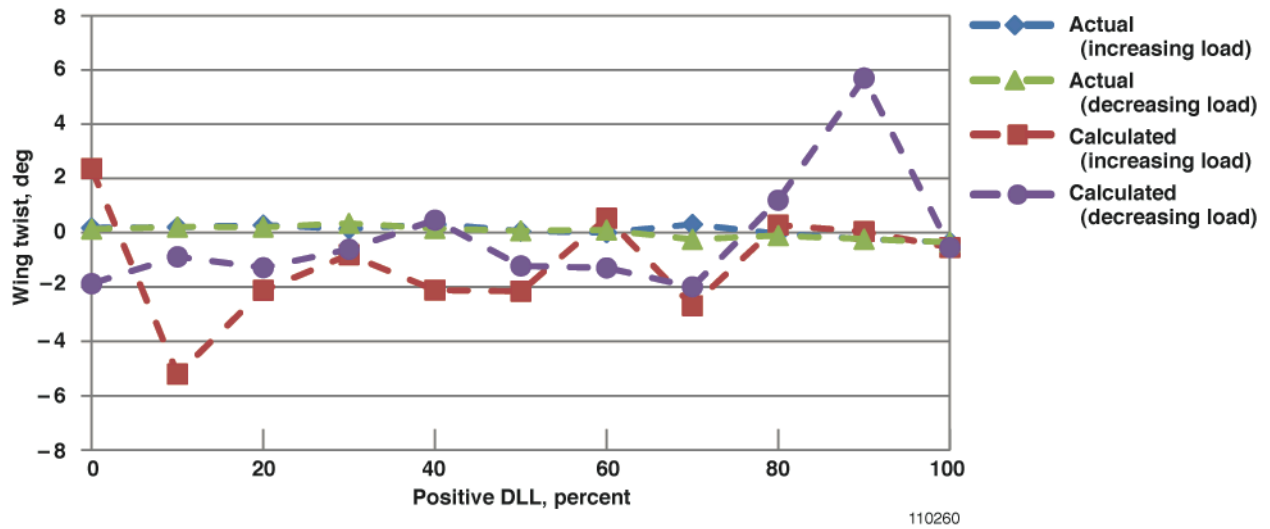
Figure 20. Wing tip twist angle errors for the span location of 1025 in. (85.4 ft) from the wing centerline for the positive load case.
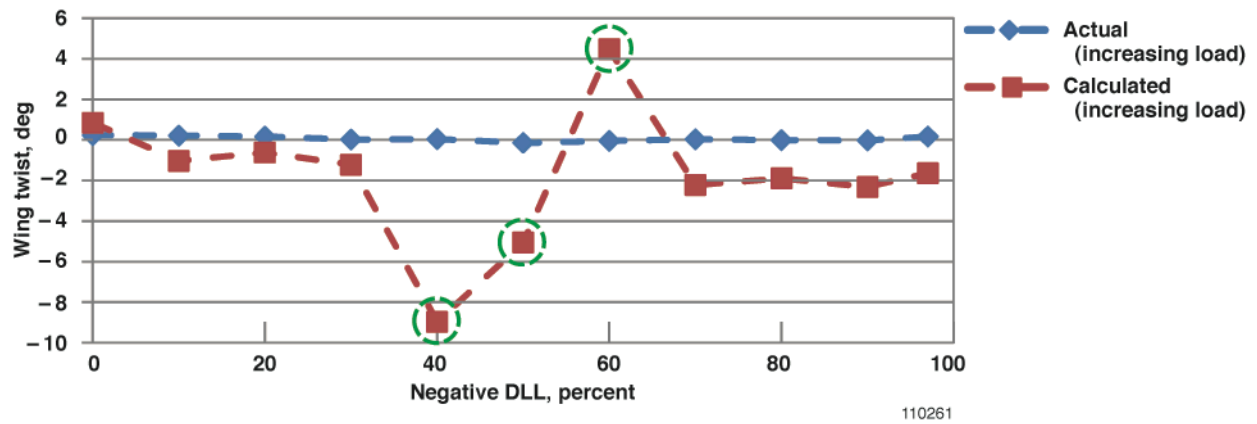
Figure 21. Wing tip twist angle errors for the span location of 1025 in. (85.4 ft) from the wing centerline for the negative load case.
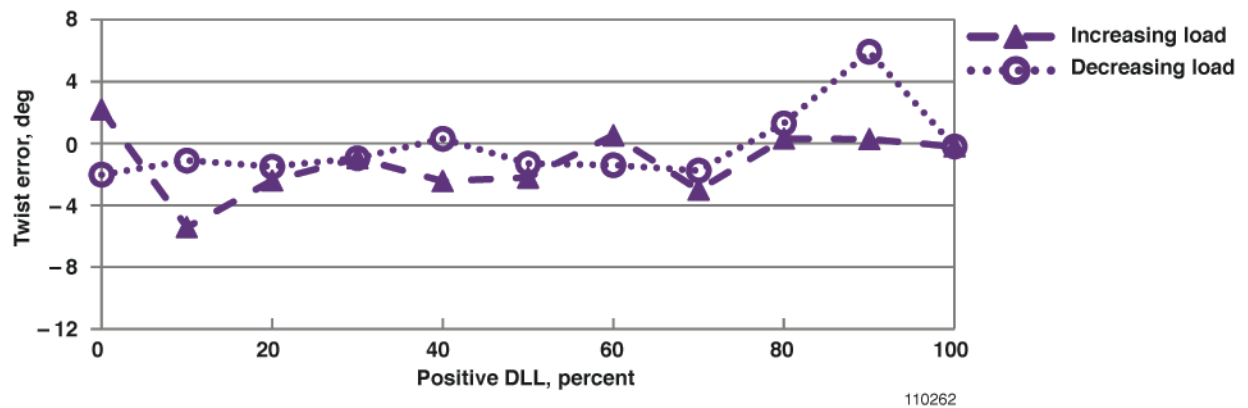
Figure 22. Wing tip twist error in degrees measured at 1025 in. (85.4 ft) from centerline for the positive load case.

34
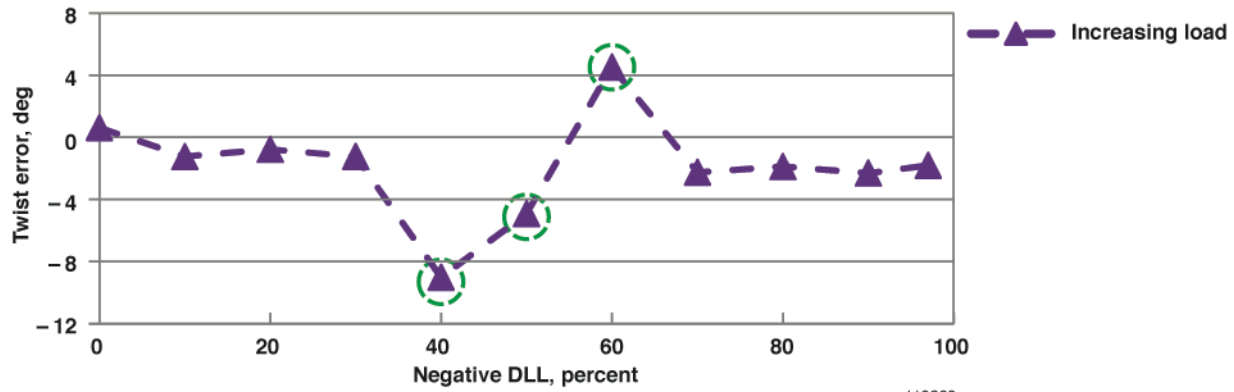
Figure 23. Wing tip twist error in degrees calculated at 1025 in. (85.4 ft) from centerline for the negative load case.
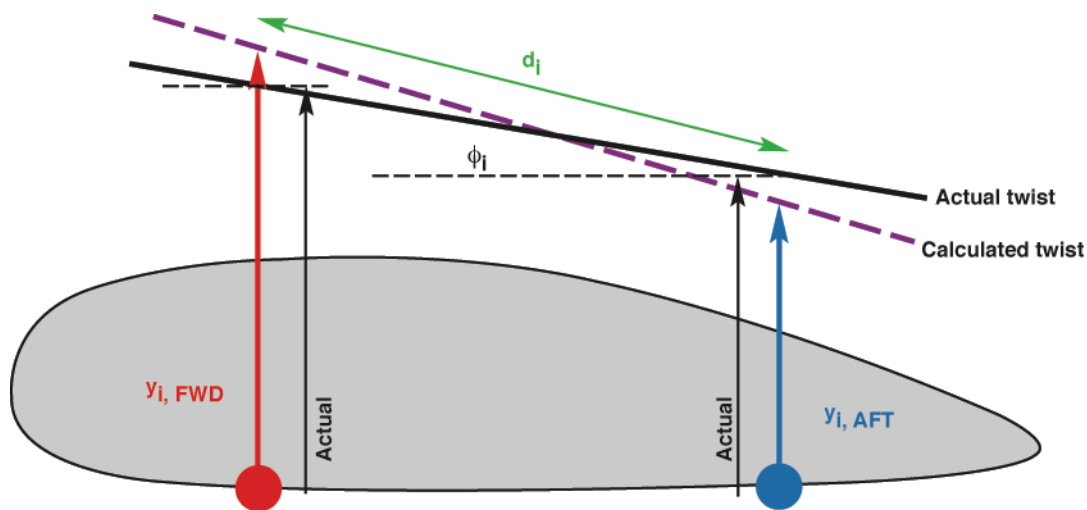
Figure 24. Illustration showing how errors in the calculated displacements ($y_{i,FWD}$ and $y_{i,AFT}$) affect the calculated twist with respect to the actual twist.
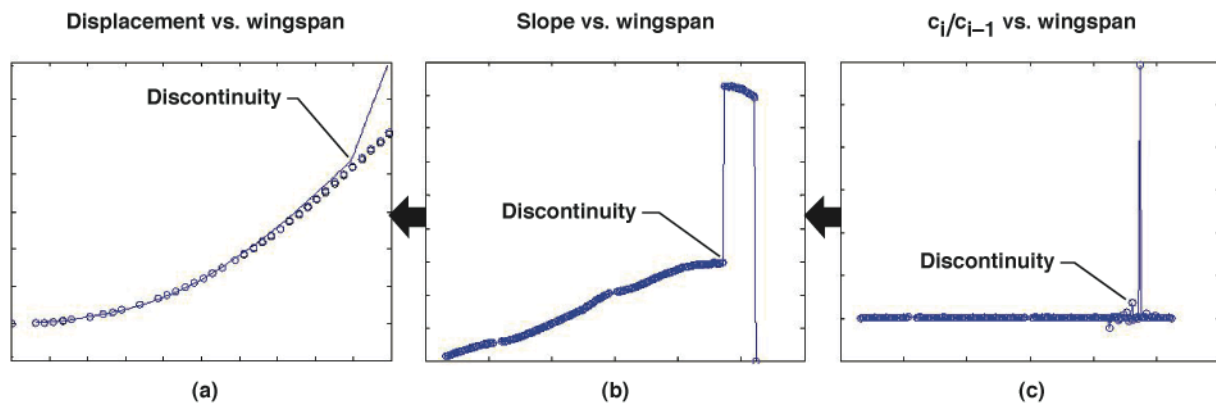
Figure 25. Illustration of how a discontinuity due to "c" values or the c-ratio value (c_i/c_{i-1}) shown in (c) can affect the slope calculation shown in (b), which in turn affects the displacement calculation shown in (a).

35
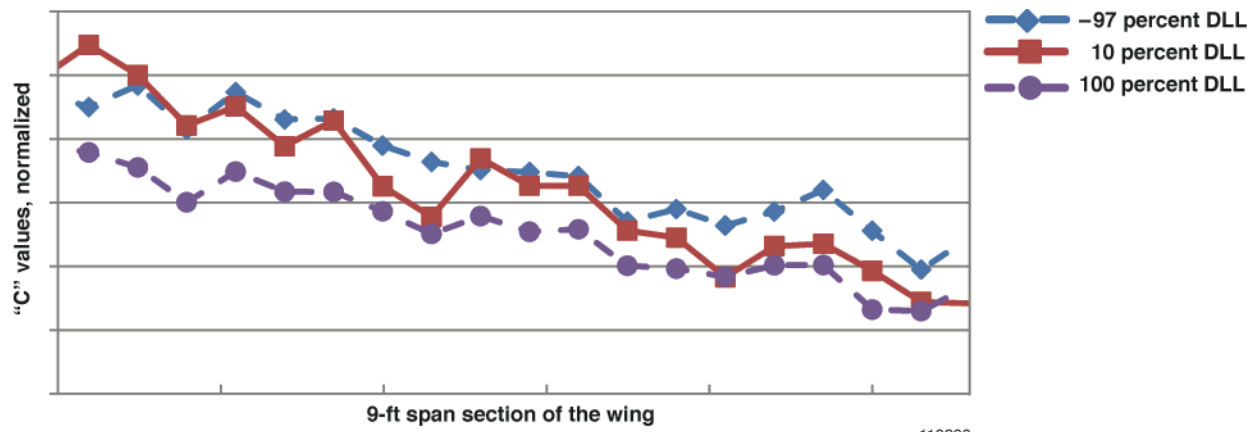
Figure 26. "c" values for various load steps over a 9-ft section of wingspan.
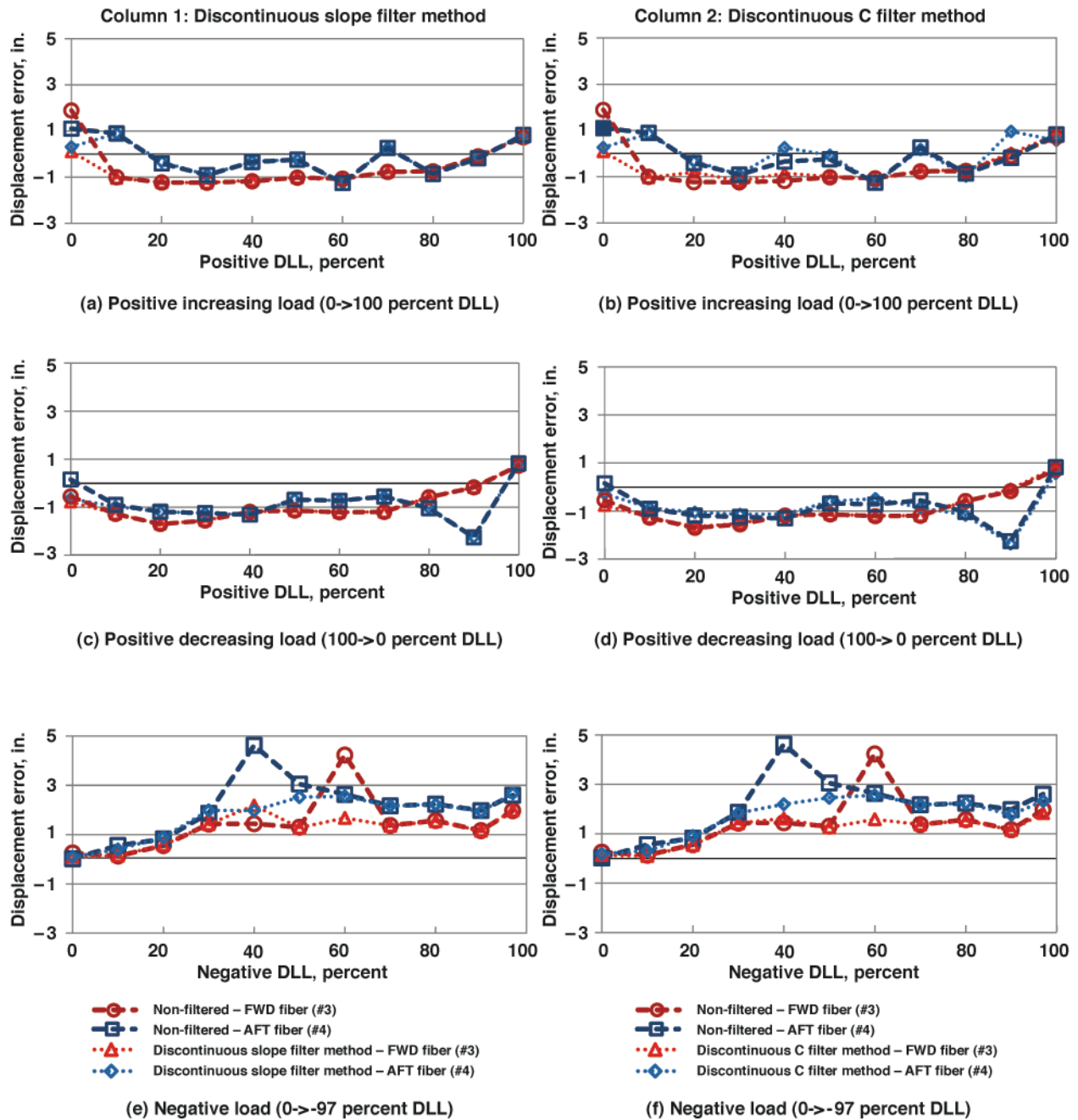
Figure 27. Comparison of wing tip out-of-plane displacement errors in inches of the Discontinuous Slope Filter method (column 1) and the Discontinuous C Filter method (column 2) to the errors when using no filtering method.
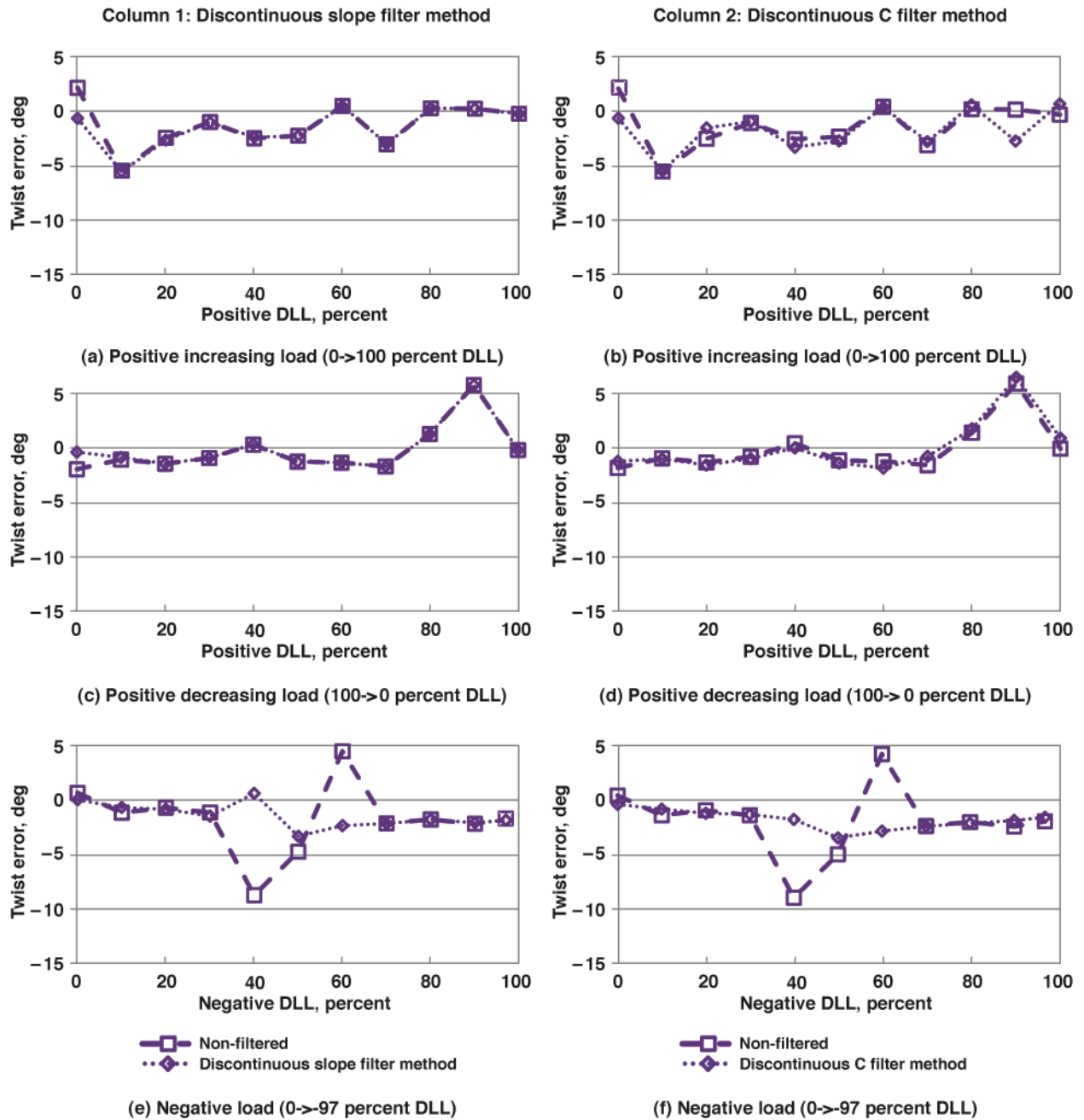
Figure 28. Comparison of wing tip twist errors in degrees of the Discontinuous Slope Filter method (column 1) and the Discontinuous C Filter method (column 2) to the errors when using no filtering method.

38

Column 1: Wing tip out-of-plane displacement

Column 2: Wing tip twist angle

(a) Positive increasing load (0->100 percent DLL)

(b) Positive increasing load (0->100 percent DLL)

(c) Positive decreasing load (100->0 percent DLL)

(d) Positive decreasing load (100->0 percent DLL)

Non-filtered – FWD fiber (#3)
Non-filtered – AFT fiber (#4)
Check load method – FWD fiber (#3)
Check load method – AFT fiber (#4)

(e) Negative load (0->-97 percent DLL)

Non-filtered
Check load method

(f) Negative load (0->-97 percent DLL)
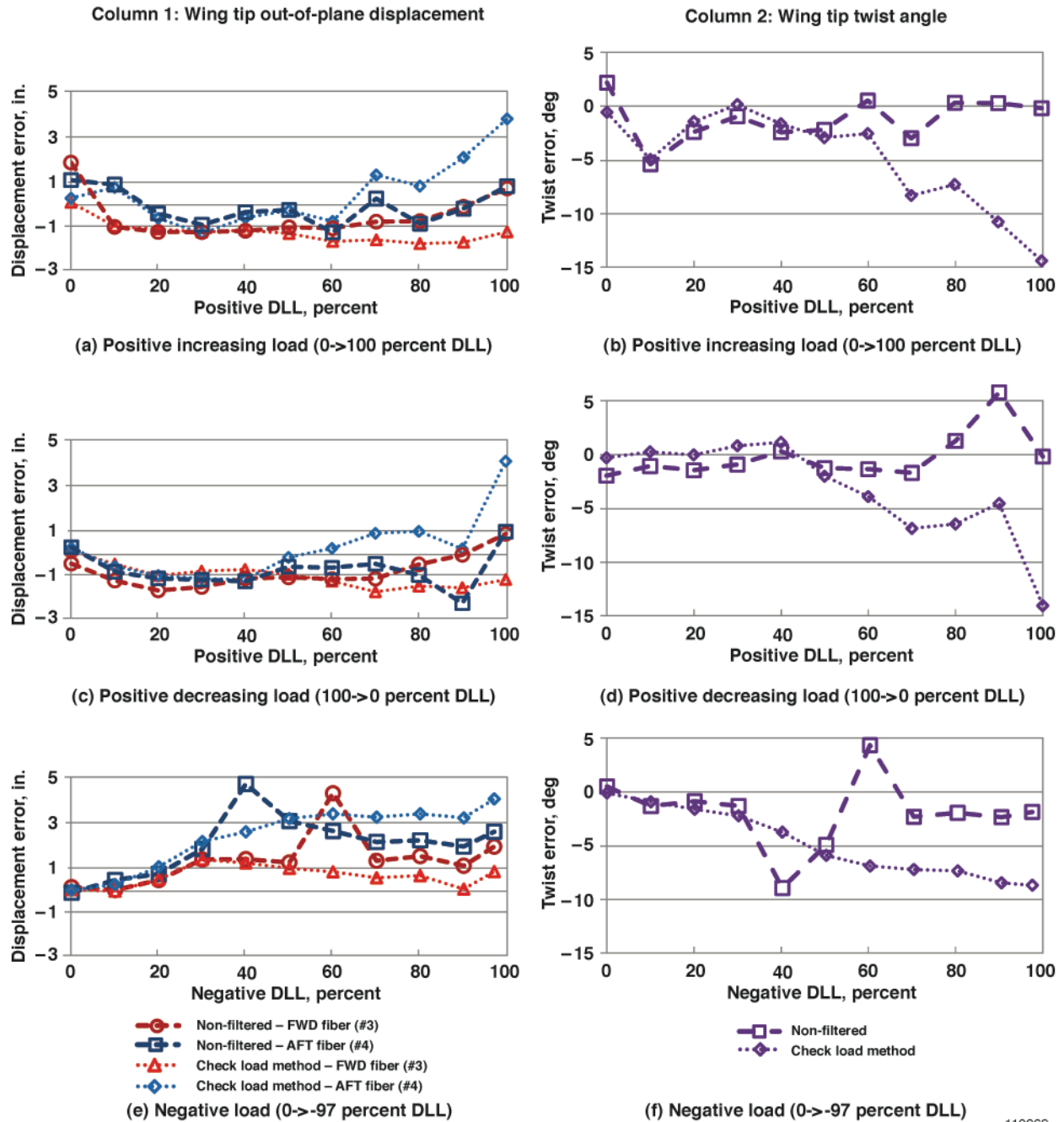
110269

Figure 29. Comparison of wing tip displacement errors and twist errors of the Check Load method to the errors when using no filtering method.

39
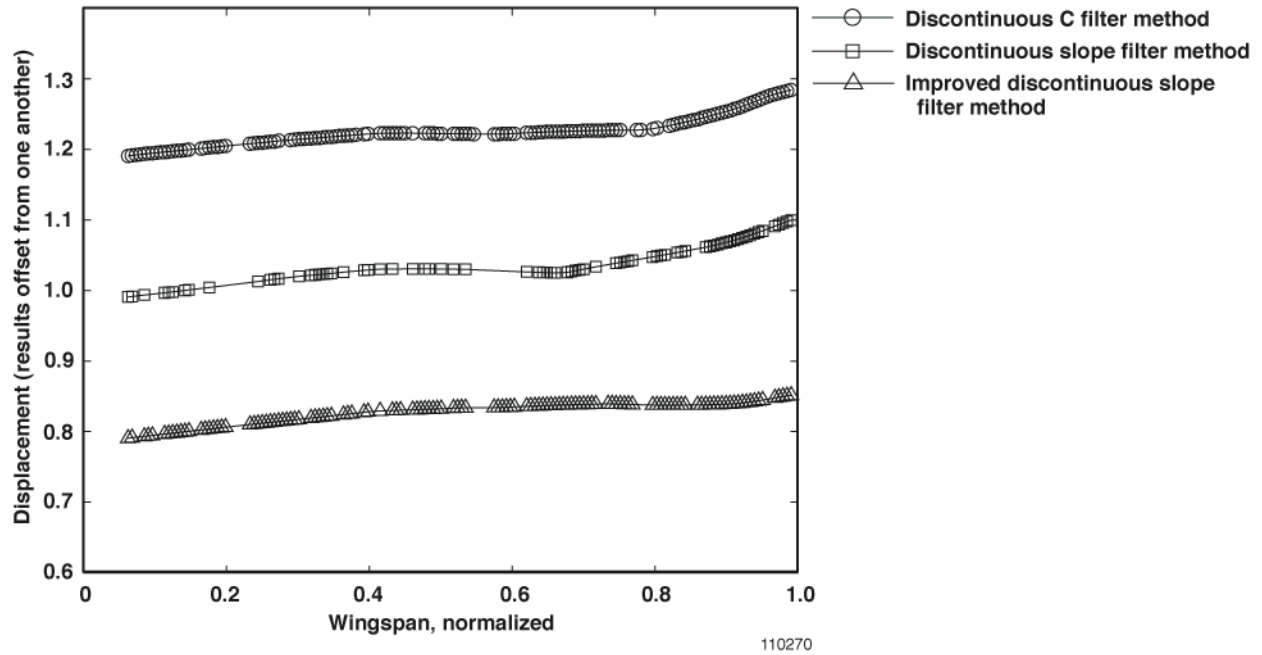
Figure 30. Remaining strain stations after three filtering methods were used to calculate the wing tip displacement at 0-percent DLL with 6 in. Δl 's.
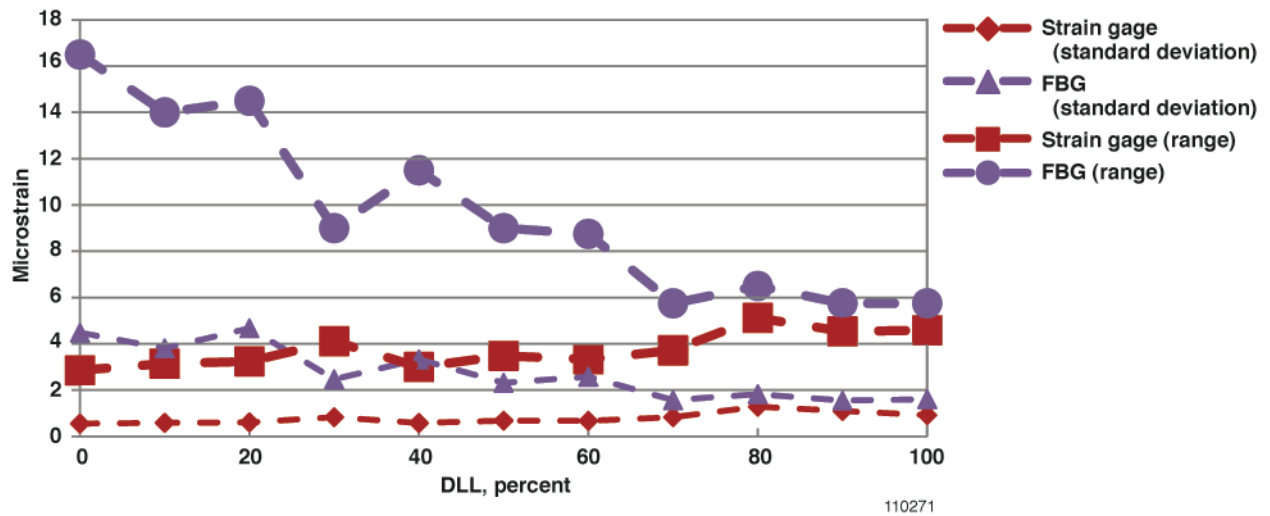

Figure 31. Comparison of the average range and standard deviation in microstrain for both strain gages and FBGs while the load increased from 0 to positive 100-percent DLL.

40
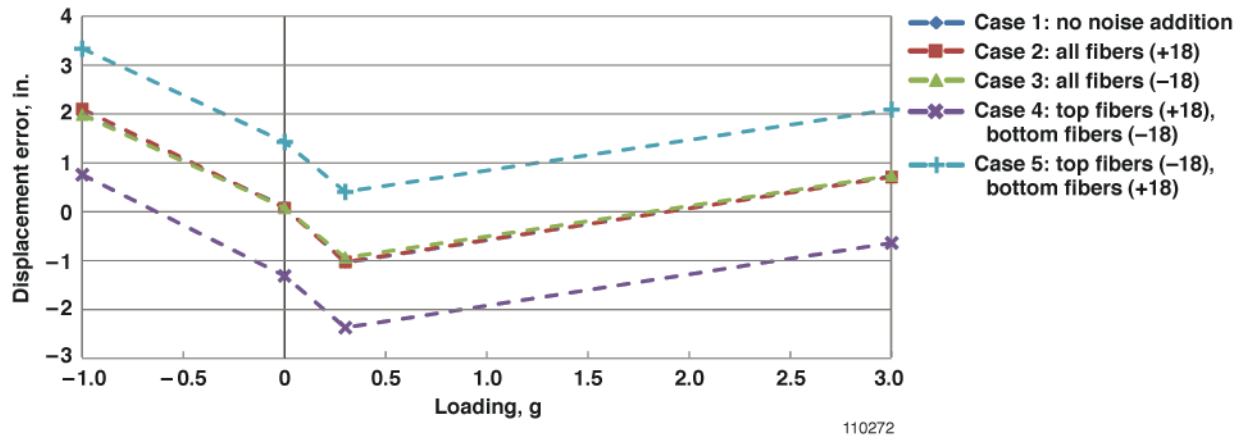
Figure 32. Wing tip out-of-plane displacement error in inches for fiber 3 when various additions of noise (in microstrain) are included in the strain values. Results with no additional noise are included for comparison.
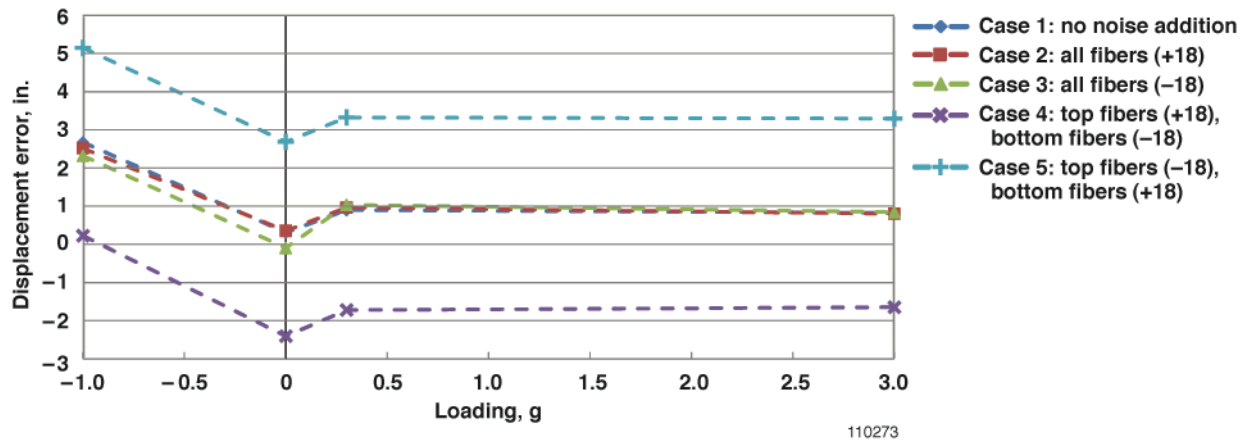

Figure 33. Wing tip out-of-plane displacement error in inches for fiber 4 when various additions of noise (in microstrain) are included in the strain values. Results with no additional noise are included for comparison.
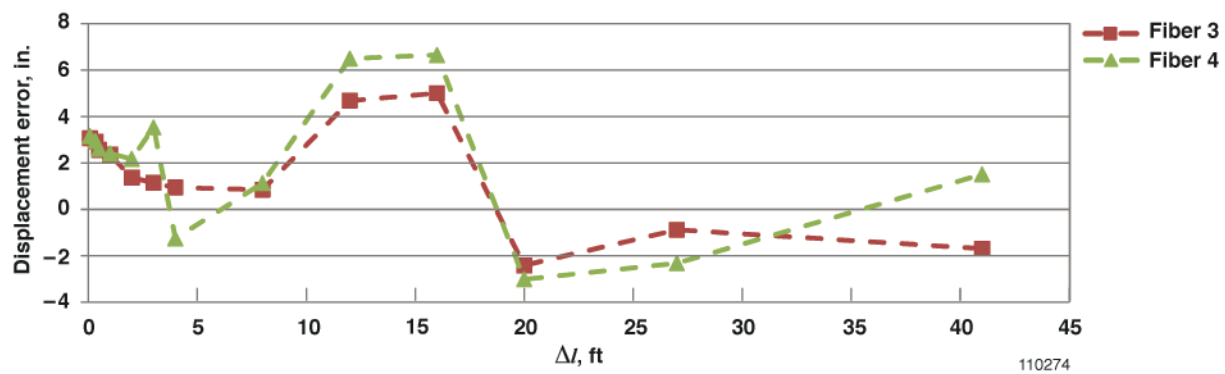

Figure 34. Wing tip out-of-plane displacement error for various lengths of Δl using data from the negative 97-percent DLL load case.
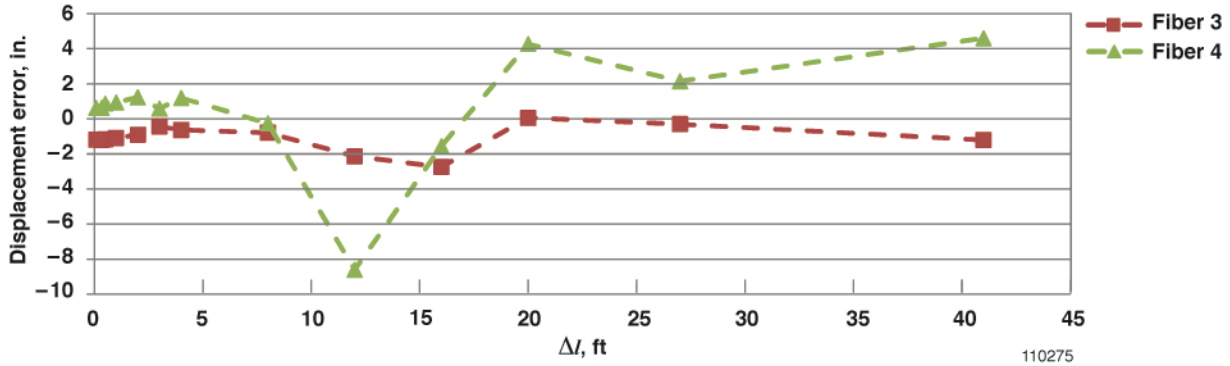
Figure 35. Wing tip out-of-plane displacement error for various lengths of Δl using data from the positive 10-percent DLL load case.
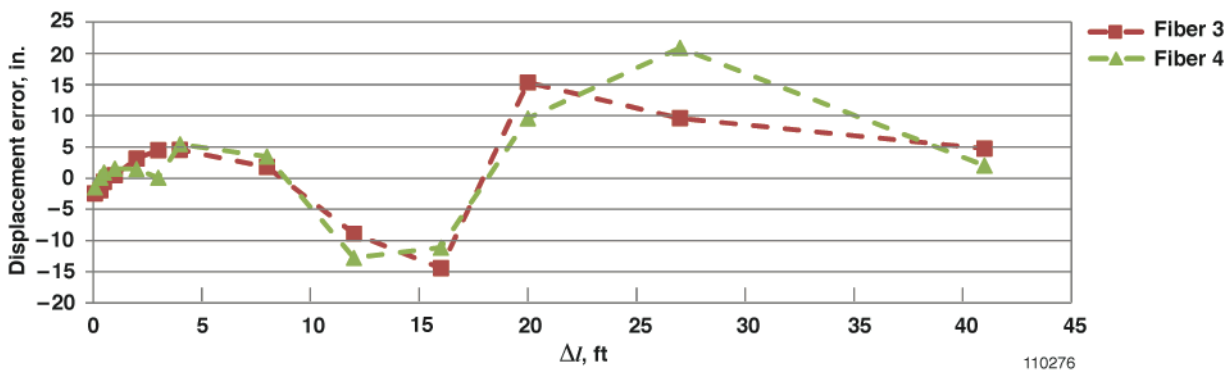

Figure 36. Wing tip out-of-plane displacement error for various lengths of Δl using data from the positive 100-percent DLL load case.
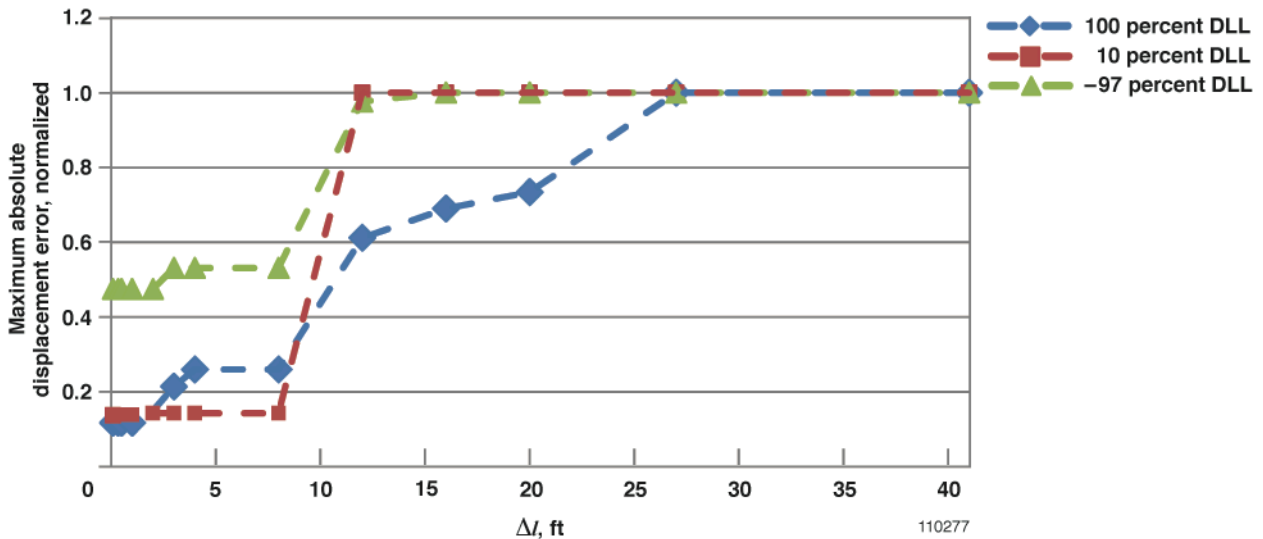

Figure 37. Comparison in the maximum absolute out-of-plane displacement errors, considering fibers 3 and 4, at the wing tip for various lengths of Δl over three different load steps (-97-, 10-, and 100-percent DLL).
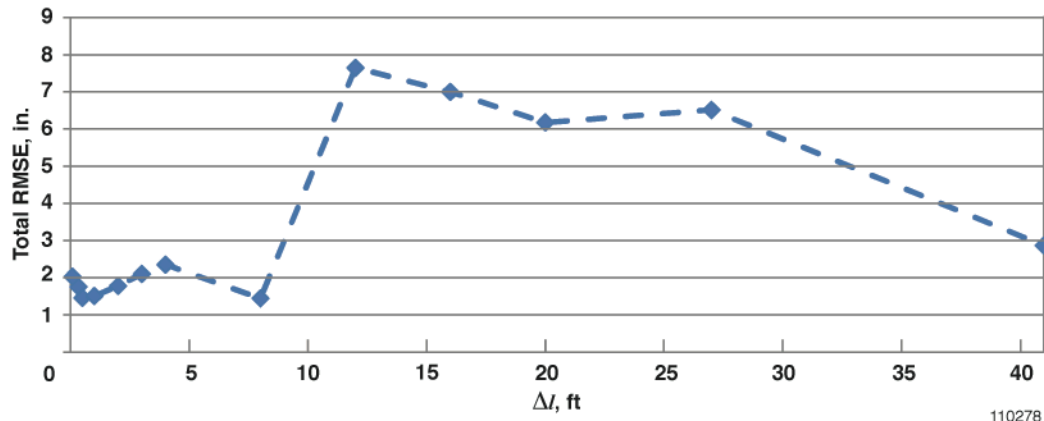
Figure 38. Total RMSE at wing tip (combines results from fibers 3 and 4 at -97-, 10-, and 100-percent DLL) for various lengths of Δl .

Appendix A
Methods for Eliminating Discontinuities

Introduction

To make the displacement equation more robust to empirical strain data, various approaches have been developed. The description of each approach is delineated below:

1. Perfect-zero Elimination
    Procedure: Eliminate problematic "c" values (for example, 0, Inf, -Inf, and NaN) due to perfect-zero strain values.

2. Curve-fit the "c" Data
    Procedure: Calculate the "c" values of the structure using the real-time, empirical strains. Fit a curve to the calculated "c" values. Use the values that fall along the curve at each strain station as "c" values for the displacement equation.

3. Predetermined "c" Values: Use a constant set of "c"-data based on a check load applied to the structure before flight.
    Procedure: Conduct a ground test to apply a check load on the structure. Determine the experimental "c" data. Assuming that the neutral axis does not shift while the structure deforms, use the experimental "c" data for all calculations of the displacement equation. This eliminates the need to calculate the "c" values in real-time. (Another approach would be to use the analytical "c" values, but that information was not available for this test, and therefore, could not be evaluated.)

4. Slope Filter: Eliminate strain stations that have "c" values that cause discontinuities in the spanwise slope calculation.
    Procedure: Calculate the slope at every strain station using the "c" values calculated from the empirical strain data. Determine at which strain stations the discontinuities in the spanwise slope calculation occur. Eliminate the strain stations (there will be two of them) that contain the "c" values causing the discontinuity in the slope equation. Calculate the displacement with the remaining strain stations. (Note: The elimination of strain stations creates larger gaps between some strain stations but is accounted for by using larger Δl s where necessary in the displacement equation. To ensure that strain stations are available over the entire wingspan, the very last strain station should never be eliminated.)

5. "c" Value Filter: Eliminate strain stations that have "c" values that are either large, small, or create a discontinuity in the spanwise calculation of the c-ratio, c_i/c_{i-1}.
    Procedure: Calculate the "c" values using the empirical strain data. Eliminate the strain stations that have "c" values that are either large, small, or create a discontinuity in the spanwise calculation of the c-ratio, c_i/c_{i-1}. Calculate the displacement with the remaining strain stations. Refer to the "Note" in the previous approach.

Five Methods for Eliminating Discontinuities

Using a combination of the approaches described above, five methods were developed to minimize the occurrence of discontinuities in the displacement equation. Each method can benefit from using approach #1 (Perfect-zero elimination). All methods, except the Check Load Method, calculate "c" values in real-time.

1. Check Load method (uses approaches #3, #1, #5, and #2).
2. Discontinuous Slope Filter method (uses approaches #1, and #4).
3. Discontinuous C Filter method (uses approaches #1, and #5).
4. Curve-fit Discontinuous Slope Filter method (uses approaches #1, #4, and #2).

5. Curve-fit Discontinuous C Filter method (uses approaches #1, #5, and #2).

Further details about the implementation of each method are included below.
1. Check Load method
    a. Apply a check load on the structure and record values over a period of time. For this work, about 20 s of strain data was recorded at 10 percent positive DLL, which corresponds to a +0.3 g loading.
    b. Calculate the time-averaged strain at each span station.
    c. Calculate the spanwise "c" values using the time averaged, empirical strain data. If necessary, eliminate problematic "c" values (for example, 0, Inf, -Inf, and NaN) due to perfect-zero strains. For this work, perfect zeros were not an issue.
    d. Detect large "c" values over the entire span, based on a chosen tolerance level (tol). Explanation of tolerances is provided below. Large "c" values were detected by first calculating the change in a "c" value from one strain station to the next and then comparing it to the average change in "c" values from previous stations. Referring to the bolded, non-italicized c-values in figure A1, the strain station affecting point D, (station (i)), is eliminated if equation (A1) is true. For this work, the tolerance (tol) equaled 10.

$$|D - C| > tol * \frac{|C - B| + |B - A|}{2} \tag{A1}$$
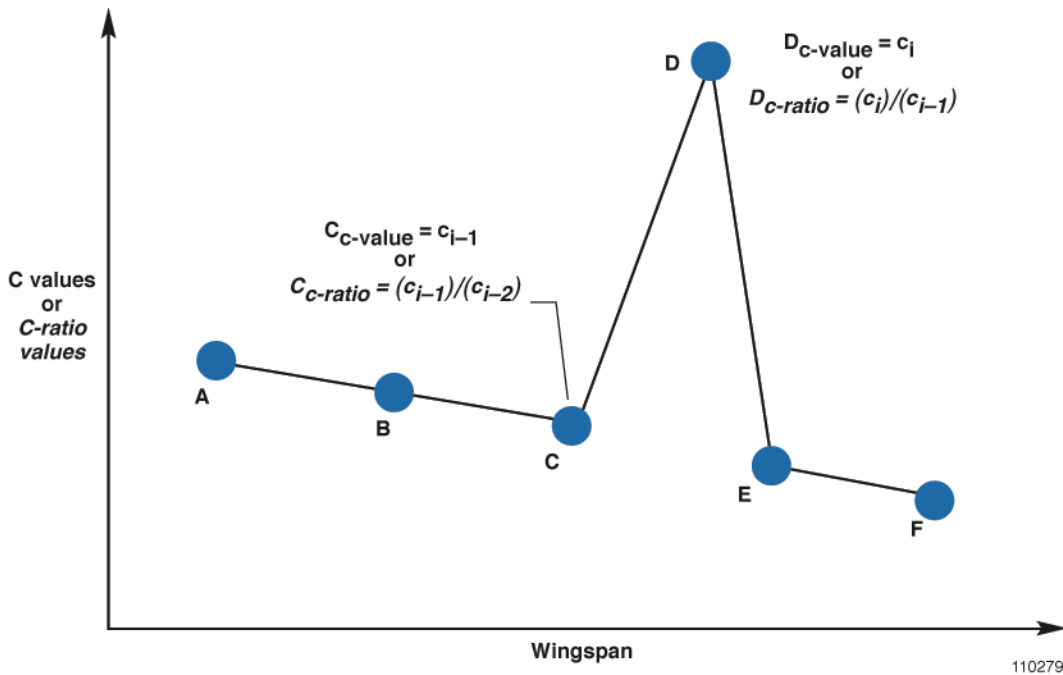
Figure A1. Detection of large "c" values or large c-ratios across the wingspan.

    e. Eliminate the strain stations having the large "c" values.
    f. Detect large c-ratio values, c_i/c_{i-1}, over the entire span, based on a chosen tolerance level. Referring to the italicized c-ratio values in figure A1, the two strain stations affecting D, (stations (i) and (i-1)) are eliminated if equation (A1) is true. For this work, the tolerance (tol) equaled 10.

45

g. Eliminate the strain stations having the large c-ratio values.

h. Curve-fit the remaining "c" data. Review the curve-fit. If the spanwise curve fit passes through zero, this means that the neutral axis exists above or below the structure for portions of the span instead of remaining within the structure for the entire span. For most wing structures, this type of curve fit is not a good representation of the neutral axis, thus choose a curve of a higher degree until the "c" data does not pass through zero, since curve fits passing though zero can create problematic c-ratio values if the "c" value close to zero falls in the denominator of the ratio. For this work, a linear curve fit passed through zero for one of the fibers; therefore, a quadratic curve fit was used instead.

i. Solve for the "c" values at each strain station along the curve-fit. Use this data for all load cases, eliminating the need to calculate "c" values in real-time.

j. Additional information:

i. No formal optimization was performed to determine the best tolerance level; however, tolerance levels of 10 and 25 were tested, and 10 was observed to be best at minimizing the displacement error.

ii. Through studies, it was noted that the c-ratio filter indirectly checks for small values in "c", making an additional check for small "c" values not beneficial.

iii. It did not always help to continue to iterate on the data until there was no discontinuities. One to two passes through the data (this method recommends two passes via steps "e" and "g") was typically optimal.

2. Discontinuous Slope Filter method

a. Calculate the spanwise "c" values using the real-time strain data.

b. Eliminate problematic "c" values (for example, 0, Inf, -Inf, and NaN) due to perfect-zero strains. For this work, perfect zeros were not an issue because the strains were time averaged.

c. Detect the "c" values over the entire wingspan that cause discontinuities in the slope calculation, based on the chosen tolerance level. A discontinuity in the slope values does not appear as a peak value but as a step increase/decrease in values. Discontinuous slopes were detected by first calculating the gradient ($m_{c,d}$) between adjacent slope values (determined from equation (A2)), and then comparing it to the average of the gradients from previous ($m_{b,c}$) and subsequent ($m_{d,e}$) strain stations. Referring to figure A2, the two strain stations affecting D, (stations (i) and (i-1)) are eliminated if equation (A2) is true. For this work, the tolerance (tol) equaled 2.

$$\left| m_{c,d} \right| > tol * \frac{\left| m_{b,c} \right| + \left| m_{d,e} \right|}{2} \tag{A2}$$

46
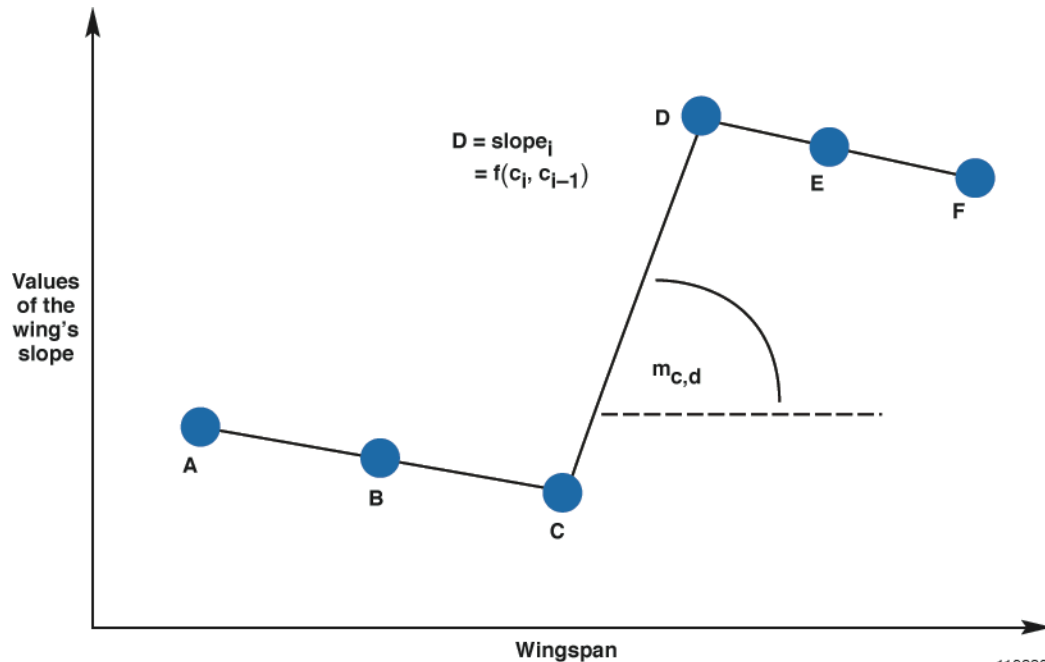
Figure A2. Detection of discontinuous slope values across the wingspan.

    d.   Eliminate the strain stations detected in the previous step.
    e.   Use the remaining strain stations in the displacement equation.
    f.   Additional information:
        i.   No formal optimization was performed to determine the best tolerance level; however, tolerance levels of 2, 5, and 10 were tested, and 2 was observed to be best at minimizing the displacement error.
        ii. It did not always help to continue to iterate on the data until there was no discontinuities. One to two passes through the data (this method recommends one pass via step "d") was typically optimal.
        iii. Also see the Improved Discontinuous Slope Filter method in the next section of this appendix.
3. Discontinuous C Filter method
    a.   Calculate the spanwise "c" values using the real-time strain data.
    b.   Eliminate problematic "c" values (for example, 0, Inf, -Inf, and NaN) due to perfect-zero strain values. For this work, perfect zeros were not an issue because the strains were time averaged.
    c.   Follow steps 'd' through 'g' in the Check Load method to eliminate strain stations having large "c" or c-ratio values.
    d.   Use the remaining strain stations in the displacement equation.
4. Curve-fit Discontinuous Slope Filter method
    a.   Execute the Discontinuous Slope Filter method.
    b.   Curve-fit the "c" values at the remaining strain stations. For this work, a cubic curve was used.
    c.   Solve for the "c" values at each strain station (using the initial, non-filtered strain stations) along the curve-fit. Use data at every strain station in the displacement equation.
    d.   Additional information:
        Steps 'b' and 'c' were added because it was perceived that curve-fitting (smoothing) the remaining "c" values, after strain stations had been eliminated, and using all the strain

47

stations which were more equally spaced would enable better displacement calculations. The assessment of these additional steps is discussed in the main report.

5. Curve-fit Discontinuous C Filter method
    a. Execute the Discontinuous C Filter method.
    b. Follow steps "b" and "c" in the Curve-fit Discontinuous Slope Filter method.

Improvements and Additional Methods Considered

Additional filtering methods were considered in this work. The Improved Discontinuous Slope Filter method and the employment of median filters are briefly discussed below.

Improved Discontinuous Slope Filter method

In one case, the Discontinuous Slope Filter method in figure 27(e) causes more error at 40-percent DLL than the non-filtered data. Further investigation showed that this method actually caused a slight discontinuity in the displacement calculation, where originally there was not one. By plotting out the spanwise slope calculation and observing the slope change near the location where the discontinuity occurred, figure A3 shows that two gradients ($m_{b,c}$) and ($m_{d,e}$) were found to have nearly the same value, such that the gradient in the middle, ($m_{c,d}$) was detected as being discontinuous. Given the slight difference in magnitude of points C and D, it is clear why this discontinuity did not cause a problem in the displacement calculation of the unfiltered data.
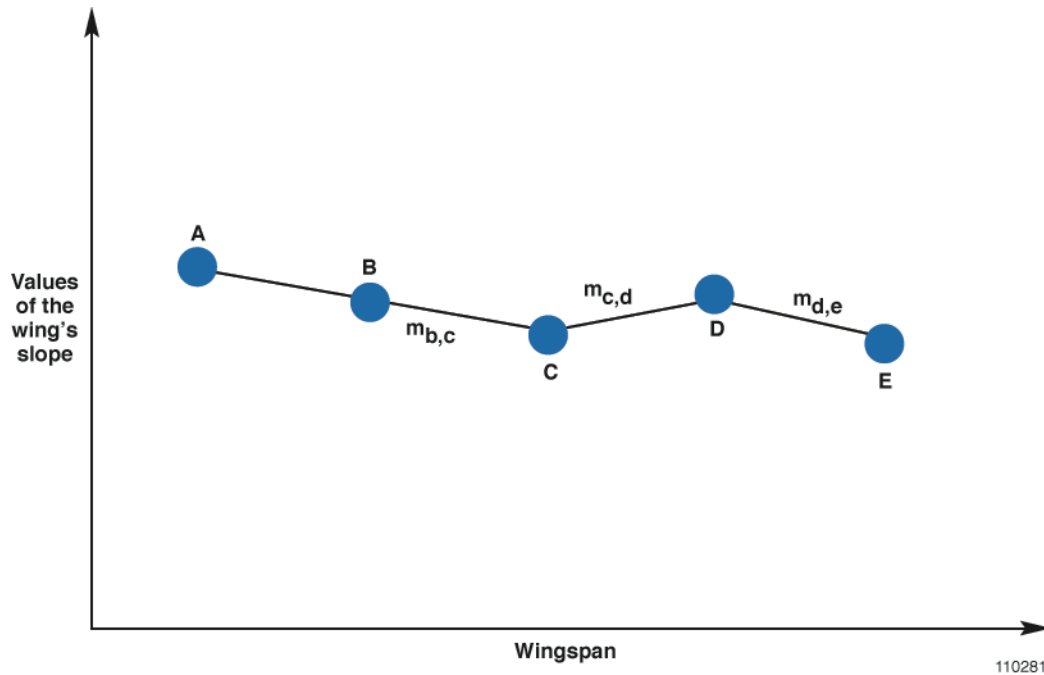

Figure A3. An example of when a non-problematic discontinuity (between C and D) in the slope calculations can be detected as discontinuous.

For this reason, it is recommended that a second condition be included in the Discontinuous Slope Filter method that once a discontinuous slope is found, the condition also verifies that there is a relatively large change in magnitude from one slope value to the next. This improvement was implemented by combining the discontinuous slope check (eq. (A2)) with a magnitude check (eq. (A1)) using an "and" statement. For the magnitude check, the tolerance level of 5 detected that the change in magnitude over the discontinuity was not problematic and did not eliminate strain stations. With a tolerance level of 2, the

48

original problem did not go away, since the slight change in magnitude was detected to be problematic, even though it was not for the unfiltered results. Using a tolerance level higher than 5 is likely to be overly conservative, such that harmful discontinuities with large jumps in magnitude would be ignored.

Median filters

Median filters were partially addressed in this work. They were first used to filter the strain values, hoping that the resulting strain values would eliminate discontinuity problems. In some cases the median filter did eliminate discontinuities, but since discontinuities in the displacement results typically occur when there are small strains, the filtering of small strains will still result in small strains. A median filter was then applied to the "c" values. Large "c" values can be eliminated in this way, but not small ones, leaving the chance for problematic c-ratio values. Applying a median filter to the c-ratio values adds complications since a c-ratio is made up of two "c" values. For the Discontinuous C Filter method, both stations that affected the problematic c-ratio were simply eliminated, but the median filters don't eliminate strain stations. Instead, the median filters may use a "good" c-ratio value over consecutive strain stations, which caused consistency problems between the "c" values and the c-ratio values. Finally, it was found that applying a median filter to eliminate discontinuities in the slope results is not straightforward, since a discontinuity in the slope results is not identified by a peak value, but by a new "plateau" of values. Further work with median filters may overcome these issues.

References

1. Ko, William L., and W. Lance Richards, *Method for Real-Time Structure Shape-Sensing,* U.S. Patent No. 7,520,176, issued April 21, 2009.

2. Ko, William L., W. L. Richards, and Van T. Tran, "Displacement Theories for In-Flight Deformed Shape Predictions of Aerospace Structures," NASA/TP-2007-214612, October 2007.

3. Ko, William L., W. Lance Richards, and Van Tran Fleischer, "Applications of Ko Displacement Theory to the Deformed Shape Predictions of the Doubly-Tapered Ikhana Wing," NASA/TP-2009-214652, October 2009.

4. Ko, William L., and Van Tran Fleischer, "Further Development of Ko Displacement Theory for Deformed Shape Predictions of Nonuniform Aerospace Structures," NASA/TP-2009-214643, September 2009.

5. Ko, William L., and Van Tran Fleischer, "Methods for In-Flight Wing Shape Predictions of Highly Flexible Unmanned Aerial Vehicles: Formulation of Ko Displacement Theory," NASA/TP-2010-214656, August 2010.

6. Richards, Lance, Dr., Allen R. Parker, Dr. William L. Ko, and Anthony Piazza, "Real-time In-Flight Strain and Deflection Monitoring with Fiber Optic Sensors," *Space Sensors and Measurements Techniques Workshop*, Nashville, TN, August 5, 2008.

7. Noll, Thomas E., John M. Brown, Marla E. Perez-Davis, Stephen D. Ishmael, Greary C. Tiffany and Matthew Gaier, "Investigation of the Helios Prototype Aircraft Mishap: Volume 1 Mishap Report," January 2004.

8. Pawlowski, Joseph W., David H. Graham, Charles H. Boccadoro, Peter G. Coen, and Domenic J. Maglieri, "Origins and Overview of the Shaped Sonic Boom Demonstration Program," AIAA-2005-0005, 2005.

9. Staszewski, Wielsaw, Christian Boller, and Geof Tomlinson, eds., *Health Monitoring of Aerospace Structures*, John Wiley and Sons, Ltd., Chichester, UK, 2003.

10. Measures, Raymond M., *Structural Monitoring with Fiber Optic Technology*, Academic Press, San Diego, 2001.

11. GOM Optical Measuring Technologies, "PONTOS-Dynamic 3D Analysis," http://www.gom.com/metrology-systems/system-overview/pontos.html, accessed September 26, 2011.

12. Stowe, David W., Douglas R. Moore, and Richard G. Priest, "Polarization Fading in Fiber Interferometric Sensors," IEEE Transactions on Microwave Theory and Techniques, Vol. 30, No. 10, pp. 1632-1635, 1982.